2011

Near Equilibrium Dissolution of Calcite Using a Flow-Through Reactor (FTR)

Michael Mante
Wright State University

NEAR EQUILIBRIUM DISSOLUTION OF CALCITE USING A FLOW-THROUGH REACTOR (FTR)

A thesis submitted in partial fulfillment
of the requirements for the degree of
Master of Science

By

MICHAEL MANTE
B.S., University of Cape Coast, 2006

2011
Wright State University

WRIGHT STATE UNIVERSITY

SCHOOL OF GRADUATE STUDIES

August 17th , 2011

I HEREBY RECOMMEND THAT THE THESIS PREPARED UNDER MY SUPERVISION BY Michael Mante ENTITLED Near Equilibrium Dissolution of Calcite Using a Flow-Through Reactor BE ACCEPTED IN PARTIAL FULFILLMENT OF THE REQUIREMENTS FOR THE DEGREE OF Master of Science.

_____

Steven R. Higgins, Ph.D.
Thesis Director.

_____

Kenneth Turnbull, Ph.D.
Chair
Department of Chemistry
College of Math and Science

Committee on
Final Examination

_____

Steven R. Higgins, Ph.D.

_____

Daniel Bombick, Ph.D.

_____

Ioana Pavel, Ph.D.

_____

Andrew Hsu, Ph.D.
Dean, WSU Graduate School

ABSTRACT

Michael, Mante. M.S., Department of Chemistry, Wright State University, 2010. Near equilibrium dissolution of calcite using a flow-through reactor (FTR)

In mineral dissolution reactions, surface morphologies play important roles particularly in near equilibrium fluids where generation of new sites of reactivity (e.g., pit nuclei) is thermodynamically disfavored. Following CO_2 injection in geologic formations, dissolution of primary carbonate minerals and crack- sealing cements will occur. The impact of these reactions on fluid chemistry requires better understanding of the reaction kinetics of major minerals at close-to-equilibrium conditions. Initial investigations have focused on quantifying calcite dissolution using short residence time (~ 10 min) flow through reactors to obtain dissolution rates at 60^{o}C, pH = 8.33 and $Pco_2 = 3.8 \times 10^{-4}$ atm. Dissolution rates decreased exponentially with time, however, the time to achieve a steady dissolution rate was approximately 120 h, suggesting that surface morphology undergoes significant changes during reaction rate decay. These observations are important in the context of the interplay between surface microtopography and reaction rates and will be discussed in light of atomic force microscopy investigations. From the experimental data in this study, the predicted relaxation time, τ is found to be ~ 30 h which is relatively larger than previous observations. The difficulty in etch pit formation and the presence of impurities is found to influence τ at very near equilibrium states

TABLE OF CONTENTS

Page

LIST OF FIGURES

LIST OF TABLES

ACKNOWLEDGEMENTS

I would like to express my profound gratitude to Dr. Steven R. Higgins for his continued guidance and sincere commitment to every stage of my research. His invaluable and wide range of knowledge in this field in helping me in every stage of this research is greatly appreciated. I also acknowledge my dissertation committee members, Dr. Daniel Bombick and Dr. Ioana Pavel for their valuable inputs and motivation. My sincere gratitude also goes to Dr. Ken Turnbull, chair of the chemistry department as well the entire staff and faculty for their immense support throughout my 2-year program. I would also like to thank Dr. Higgins research group: Dr. Man Xu, Brittany Campbell, Mike Smith and Dennis Lennaerts for their support and encouragement. I owe my sincere thanks to the United States Department of Energy, Office Science, Basic Energy Sciences, Chemical Sciences, Geosciences and Biosciences Division and the National Science Foundation Instrumentation and Facilities program who provided all the financial support in carrying out this research. Special thanks also go to the collaborators of Dr. Higgins research, the Livermore National Laboratory, especially Dr. Kevin Knauss for their expertise.

Finally I would like to thank my parents and entire family for every investment put in me throughout my academic life. Their encouragement, care and support cannot be overemphasized.

Chapter 1

Introduction

Mineral dissolution is fundamental to most geochemical and biological processes but the lack of a general dissolution model makes it difficult to fully understand the overall dissolution of rock forming minerals such as calcite and variation of reaction rates with environmental conditions. Calcite serves as one of the most important biominerals and plays a significant role in the CO_2 cycle and CO_2 emissions influences the concentration of CO_2 in the atmosphere over 10^5-10^6 y timescales (Brantley, 1995) and this has necessitated the need to find solutions to counter rising atmospheric CO_2 to maintain the balance in the carbon cycle. With the emergence of CO_2 sequestration in recent times as one of the methods proposed by researchers (Bachu, 2000) to seek to lower the increasing amount of CO_2 in the atmosphere, the dissolution rate of calcite and the controlling factors has been a research area of keen interest. Calcite exists over a wide range of intermediate depths in most geological aquifers where CO_2 injection may take place (Caldeira, 2000). The reaction kinetics between aqueous solutions and calcite are therefore important to the initial and long-term fluid and mineralogical changes in these formations and attempts have been made in laboratories to model the kinetics of calcite dissolution at various saturation states (e.g., Morse et al, 2007).

The relevance of carbonate mineral dissolution dates all the way back in the 1800s when investigators such as Murray and Renard (1891) started uncovering and studying the formation and dissolution of carbonate minerals. The study of these minerals became more prominent in later years (Weyl, 1958; Friedman, 1964; Berner, 1967; Berner and Morse 1974; Morse and Mackenzie 1990) when significant efforts were employed to

experimentally study reaction rates of carbonates. Rates of release of solutes from minerals into aqueous solution are often used to calculate the dissolution rate and factors such as pCO_2, solution pH, temperature, foreign ions and molecules, solution saturation state, (Ω) and surface morphology have all been found to influence reaction rates.

Dissolution reactions are described as either being diffusion controlled or surface controlled. In a model for crystal growth commonly referred to as the Burton, Cabrera, and Frank (BCF) model proposed by Burton et al. (1951), when adsorption of reactants on the solid surface occurs, followed by migration of the reactants on the surface to an "active" site such as a kink site along a step edge, chemical reaction between the adsorbed reactant and solid occurs where bonds are formed and broken. The products formed as a result migrate away from the reaction site and when desorption of products to the solution occurs the dissolution process is described as surface controlled. On the other hand, if dissolution occurs with diffusion of reactants through solution to the solid surface, followed by the steps outlined for surface controlled dissolution and finally diffusion of products away from the surface to the bulk solution, then the dissolution is considered as diffusion controlled.

According to the literature (Sjoberg, 1978; Plummer et al. 1978; Rickard and Sjoberg 1983; Busenberg and Plummer, 1986; Chou et al, 1989; Schott et al, 1989a; Shiraki et al, 2000; Alkattan et al, 2002), pH determines whether the calcite dissolution rate is surface controlled or diffusion controlled. The authors observed that at $pH < 3.5$, dissolution is to be diffusion controlled whereas at $pH > 3.5$, a surface controlled mechanism of dissolution is observed. Hence dissolution of calcite is influenced by H^+ activity and in a higher pH region, the rate of detachment of ions becomes more dependent on solution

chemistry and pCO_2. Considering the effect of pCO_2 on calcite dissolution, Plummer et al. (1976), observed that in slightly acidic to circumneutral solutions, (pH = 4-5) containing 0.003-0.037 M $NaHCO_3$ at 25 to 60^oC, the dissolution rate increased by a factor of 5 to 10 when the pCO_2 increased from 1 to 50 atm. However at 100^oC there is a systematic increase in rate from 1 to 30 atm but decrease between 30 and 50 atm. The dissolution of calcite with regards to pCO_2 therefore varies directly with temperature, (T) at $T \leq 60^o$ C but inversely at $T \geq 60^o$ C.

Arrhenius plots of dissolution rate constant, (ln k), as a function of temperature, (1/T), generally indicates that the rate limiting step changes with temperature, and dissolution reaction may change from surface controlled at low temperatures to diffusion controlled at high temperatures since the activation energy of interface reactions is larger than the activation energy of transport. Gutjar et al. (1996) recorded a high activation energy (35 kJ/mol) in near equilibrium conditions and realized that the reaction order, n in equation (1), changed from 2 at 20^oC to 1.2 at 70^oC with the rate constant increasing by a factor of 2. From a study by Sjoberg and Rickard (1984) where carbonate dissolution was studied with regards to temperature influence, the boundaries between H^+ dependent, transitional and H^+ independent regimes were found to move to lower pH values with increasing temperature.

Foreign ions, mostly divalent cations such as Sr^{2+}, Mn^{2+}, Mg^{2+}, phosphates and organics also pose significant effects on calcite dissolution according to investigators (Weyl, 1958; Terjesen et al, 1961; Berner and Morse, 1974; Gutjahr et al, 1996a;). These inhibitors retard dissolution substantially via their attachment to active sites such as kinks, causing step pinning.

The most commonly used equation in mineral dissolution is

$$\text{Rate} = k(1-\Omega)^n \qquad (1)$$

where k, Ω and n refers to rate constant, saturation state and rate reaction order respectively. Apart from the above mentioned factors, the equation above indicates that, calcite dissolution is also driven by solution undersaturation. Dissolution is favored in lower saturation conditions ($\Omega < 1$) but disfavored at higher saturation states ($\Omega > 1$) and previous experiments (Sjoberg and Rickard 1983) indicate that dissolution rates increase with decreasing Ω as can be inferred from the above equation.

Morse (1974a) indicated that the rate of dissolution under any given conditions was linearly proportional to the surface area of a given sample used. Reactive surface areas which in part relates to crystal defect density such as steps and etch pits (Schott et al, 1989) has been found to be one important factor that influences dissolution rate in that surfaces with higher defect density undergo rapid rates of dissolution. Later experiments by MacInnis and Brantley (1992) also suggested that etch pit size variation and distribution influences dissolution rates of calcite and determined steady state rates (3.1×10^{-10} mol $cm^{-2}s^{-1}$) to be 3 times higher than rates reported by Plummer et al. (1978) and Chou et al. (1989). The observation by MacInnis and Brantley (1992) was that steeply inclined surfaces found on the walls of etch pits ultimately influenced the overall dissolution rate.

Atomic Force Microscopy (AFM) studies (Liang et al, 1996a, 1996b; Liang and Baer 1997; Lea et al, 2001; Teng, 2004; Bose, 2008), where dissolution of minerals is studied at the atomic scale provides evidence on the effect of surface morphology on reaction

rates where movement of steps are tracked during the dissolution process of calcite and subsequently found to impact the rate of dissolution. From the AFM studies, etch pits observed on the mineral surface as a result of dissolution were found to deepen and widen and eventually coalesce in far from equilibrium saturation states. The overall dissolution process is thus controlled by processes such as etch pit growth and subsequent pit-pit overlap as well as step migration whose velocity is a function of the crystallographic orientation of the step.

To better understand mineral-fluid reactions associated with CO_2 sequestration and their long term effect in geologic systems, reactions at the interface between mineral surfaces and aquifer fluids in which the gas is dissolved must be closely studied. CO_2 forms a quantitavely solvated molecule, CO_2 (aq) and carbonic acid in aqueous solution wherein carbonic acid subsequently undergoes partial dissociation to form carbonate and bicarbonate, thereby initially decreasing fluid pH. The increased proton activity enhances the dissolution of most formation minerals, including calcite, resulting in progressive neutralization of the acid and the release of metals into the aqueous solution. Eventual increases in fluid alkalinity from dissolution of silicates create fluid supersaturation in some divalent metal carbonates leading to the eventual precipitation of these minerals. While this sequence of reactions is a vast oversimplification, ignoring not only physical transport processes but also the mineralogical and fluid chemical diversity of real formations, it captures the basic reactions expected to take place in a mineral-trapping chemical pathway to CO_2 sequestration. One key objective for modelers of pilot and full-scale injection sites is to predict the time-scales over which various chemical and physical processes are operative. In order to develop these models in a realistic manner,

detailed information on rate processes is required. In the present work, the emphasis is on dissolution processes at the calcite-water interface.

Generally, the overall dissolution of calcite in the presence of CO_2 is described in the reaction below:

$$CO_2 + H_2O + CaCO_3 \rightarrow Ca^{2+} + 2HCO_3^-$$

The rate of dissolution is dependent on temperature, the saturation state of the solution, the concentration of dissolved CO_2 (implicit pH-dependence) and in some cases, the preparation and history of the calcite mineral. Atomic Force Microscopy (AFM) experiments enable the observation of topographic changes to the mineral surface as dissolution occurs, providing the ability to probe the effects of the aforementioned quantities on surface kinetics. Other than the effect of pCO_2 and solution pH on "steady-state" dissolution rates earlier reported by Pokrovsky et al. (2002), sample surface topography may have a major influence on the rates of reaction prior to attainment of this so-called "steady-state" rate. In this work, "steady-state rate" will not be used, but instead we will use "steady rate" as the latter is defined phenomenologically to be the constant rate observed after a sufficiently long period of reaction whereas the former, in chemical convention, is an approximation based on intermediate concentrations, which are usually unknown quantities in mineral dissolution experiments. In addition to topographic effects on "transient" dissolution rates, solution chemistry is hypothesized to influence the duration, or decay time, of the dissolution transient through its well-known effects on the rates of reaction at elementary step edges. A simple model for the topographic decay of mineral surfaces during dissolution in near-equilibrium fluids,

described by Bose et al. (2008) wherein step speeds and rate decay times are inversely related, forms the basis for this hypothesis. Although an enormous amount of data exists on calcite dissolution (Berner and Morse, 1974; Plummer and Wigley, 1976; Dreybrodt, 1981b; Schott et al, 1989; MacInnis and Brantley, 1992, Morse and Arvidson, 2002), an insufficient understanding of the processes leading up to the attainment of a steady rate hampers the development of fundamentally-sound reactive transport codes for modeling geologic CO_2 sequestration.

As indicated above, dissolution is driven by solution undersaturation (Gledhill and Morse 2004) and researchers have largely focused on conditions far from equilibrium (Giudici et al, 2002; Lasaga and Lüttge, 2001). Recognizing that near-equilibrium conditions are likely to obtain in long-term geologic sequestration, we designed calcite dissolution experiments using a short residence time flow through reactor (FTR) at 60 ^{o}C in near-equilibrium solutions to study the effect of sample history on dissolution rate, to understand and discern relative solution saturation on dissolution rate and to investigate surface morphology evolution during dissolution.

Chapter 2

Experimental

2.1 Materials

Calcite crystals were synthesized using a procedure reported previously by Paquette and Reeder (1995). The calcite crystals used for these experiments were grown in an aqueous solution of deionized water (18.2 MΩ-cm resistivity) containing 0.0065 M Ca^{2+}, from $CaCl_2$-$2H_2O$ (ACS grade), and 0.50 M NH_4^+, from NH_4Cl (ACS grade), in a sealed glass cylinder (1.9 L internal volume) using Teflon caps at both ends. The container was then placed into a temperature-controlled bath maintained at 40°C and allowed to stabilize overnight. The following day a bottle containing $(NH_4)_2CO_3$ (ACS grade) was attached to the container through a small opening in the top Teflon cap, separated from the solution headspace by filter paper placed between the bottle and the opening to ensure that no particles of $(NH_4)_2CO_3$ contacted the solution but permeation of the gaseous NH_3 and CO_2 could occur during decomposition of the salt. The container was then maintained at 40 °C and crystals usually were observed after 5 days and after 16-30 days, the crystals were collected. The solution containing the calcite crystals was filtered through Whatman 1 filter paper, the container was rinsed using ethanol so not to dissolve any remaining crystals, and the crystals were then rinsed with and stored in ethanol until use.

2.2 Material Characterization

To determine the size of the crystals produced, a batch of the crystals was sampled and photographed using a digital camera adapted to a Leica S6D optical microscope. An

average crystal size for the synthesized sample was found to be 360 ± 90 μm. Another batch of crystals of mean size 160 ± 52 μm was synthesized in the same way as before. However, unlike the former, the relatively smaller crystals (160 μm) were collected after 5-6 days of synthesis. In calculating geometric surface area (A_p), a statistical approach was adopted where surface areas of crystals (rhombic shape assumed) of particular sizes were determined together according to equation (2). The mass of the measured particles (m_p) was calculated using equation (3). Knowing the mass of the sample weighed, m_s, the statistical mass determined, and the surface area calculated in equation (2), the total surface area (A_{tot}) of the experimental sample was obtained according to equation (4). The uncertainty in surface area was insignificant in comparing data points within a particular experiment and even in comparing one experiment to another using similar crystal samples. The uncertainty in surface area was however ~ 25 % and ~ 34 % for the larger and smaller crystals respectively in the determination of dissolution rates.

$$A_p = 6 \sum_{i=1}^{M} N_i l_i^2 \quad (2)$$

$$m_p = \rho \sum_{i=1}^{M} N_i l_i^3 \quad (3)$$

$$A_{tot} = \frac{m_s}{m_p} \times A_p \quad (4)$$

Where: ρ is the density of calcite (2.71 g/cm^3)

N_i, the number of particles of the same size in a particular subset of particles

l_i is the particle size of a given subset of the sampled particle population.

M is the number of subsets used to generate the particle population histogram.

Fig. 2.1 and 2.2 shows histograms of the smaller crystals (~ 100 crystals) and larger crystals (~ 50 crystals) respectively where the size of the calcite crystals is plotted as a function of crystal population. Both histograms have the bin size to be 0.01 mm. The average crystal size is 0.16 mm (160 µm) for the smaller crystals. In Fig. 2.2, where the crystals are larger, the most populated crystal is within the range of 0.30 mm – 0.40 mm and the least populated crystals is in the range of 0.10 mm – 0.20 mm and 0.50 mm – 0.60 mm. The average crystal size is calculated to be 0.36 mm (360 µm) for the larger crystals.

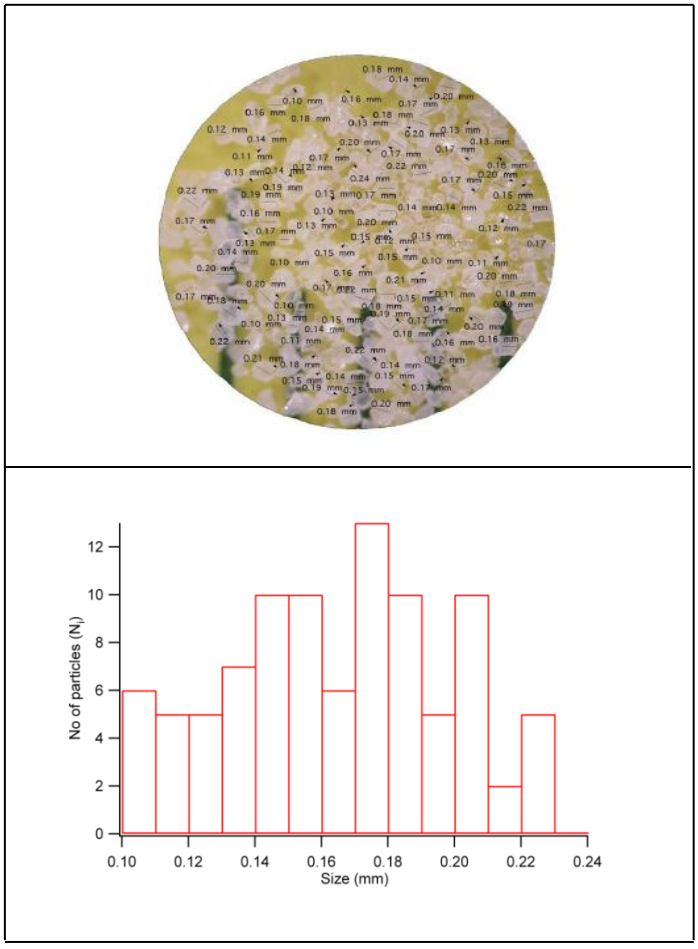

Fig. 2.1: A histogram (below) showing the distribution of calcite crystals (above) of mean size 160 µm

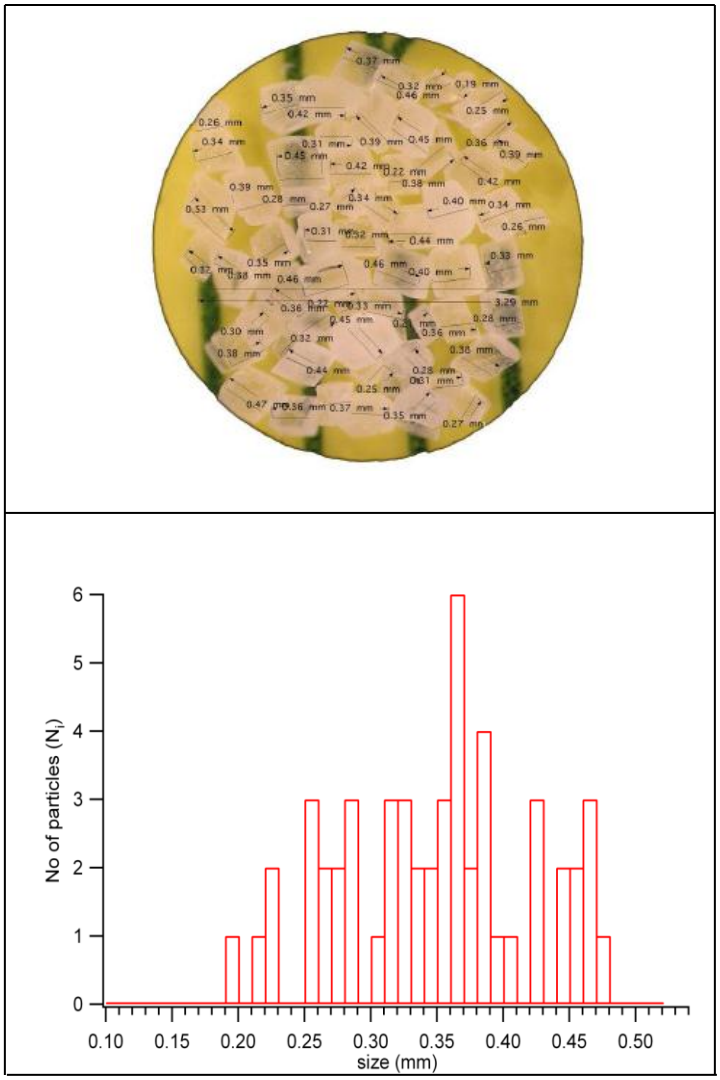

Fig. 2.2: A histogram (below) showing the distribution of calcite crystals (above) of mean size 360 µm

Using the Atomic Force Microscope (AFM), images of the crystals used in the experiments were taken before and after experimental runs. Crystals were selected from a batch and placed on a gold-coated mica substrate and mounted on the microscope stage of a Molecular Imaging PicoPlus AFM. Samples were initially imaged using contact mode AFM and Nanosensors PPP-CONT cantilevers with nominal spring constants of 0.2 N/m; however, due to the roughness of the calcite surfaces, intermittent contact mode

was used after excessive tip wear occurred when scanning the surfaces in contact mode. For intermittent contact mode, PPP-NCH (Nanosensors) cantilevers were used. Images were acquired at a range of lateral scales to map both the smallest resolvable surface features as well as to identify long range characteristic surface features and for performing quantitative surface analysis.

2.3 Solution Preparation

Using Visual MINTEQ, the solution composition was determined for a targeted saturation state, Ω. The saturation state is defined as;

$$\Omega = \frac{(Ca^{2+})(CO_3{}^{2-})}{K_{sp}(\text{Calcite})} \qquad (4)$$

where (Ca^{2+}) and ($CO_3{}^{2-}$) are the calcium and carbonate activities respectively and K_{sp}, the solubility product of calcite. MINTEQ calculations for the solution preparation were computed open to CO_2 in air as seen in Table 2.1. A 0.01 M $CaCl_2$ stock solution was prepared by dissolving 1.470 g of $CaCl_2.2H_2O$ (A.C.S reagent grade) in a clean 1 L volumetric flask using deionized water. Another solution was prepared but this time by dissolving 0.109 g of $NaHCO_3$ in deionized water contained in a clean l L volumetric flask to make 1.3×10^{-3} M $NaHCO_3$. To get the concentration of $CaCl_2$ needed for a particular Ω according to Table 2.1, a known volume of the $CaCl_2$ solution taken from the stock was mixed with bicarbonate solution in a 1 L volumetric flask. The solution was then poured into a 4-necked round bottom flask which served as the reservoir for the experiment (Fig. 2.3). At room temperature (25 ^{o}C) the predicted pH from MINTEQ was

found to be higher than the measured pH. While the kinetics of CO_2 equilibration with aqueous solutions are known to be relatively rapid from previous work (Wissbrun et al, 1954; Patel et al, 1972), the discrepancy between measured and predicted pH may indicate slow CO_2 degassing of the experimental solutions which, as prepared with $NaHCO_3$, are initially supersaturated in dissolved CO_2 based on the thermodynamic database used by Visual MINTEQ. Similar calculations performed using EQ3/6 verified consistency across thermodynamic modeling platforms.

Table 2.1: Experimental Solution Composition Data

Expt.	mass($NaHCO_3$)/g dissolved in 1L DI H_2O	[$NaHCO_3$] mol/L	Vol.($CaCl_2$) stock/mL	[$CaCl_2$] mol/L	Calc. pH at 60 °C	Calc. pH at 25 °C	Measured pH at 25 °C	Ω at 60 °C
1	1.09E-01	1.3E-03	1.0	1.0E-05	8.55	8.33	8.15	0.12
2	1.09E-01	1.3E-03	1.2	1.2E-05	8.55	8.33	8.18	0.15
3	1.09E-01	1.3E-03	2.0	2.0E-05	8.55	8.33	8.14	0.25
4	1.09E-01	1.3E-03	2.6	2.6E-05	8.55	8.33	8.12	0.32
5	1.09E-01	1.3E-03	4.6	4.6E-05	8.55	8.32	8.11	0.56

2.4 Experimental Apparatus

The solution temperature was kept at 60 °C using a heating mantle, thermocouple and temperature controller. To ensure that the input solution equilibrated with air, a gas cylinder containing compressed air was bubbled through the reservoir. A condenser was also connected to the reservoir to prevent evaporation. The reservoir solution was continuously stirred with a stir bar to ensure a homogenous solution. Using a Kloehn syringe pump, the solution was pumped through the cell with a constant flow rate of 3.40 ± 0.03 ml/hr. The flow through reactor cell made of stainless steel with internal volume of 0.06 ml was sealed at both ends with frits (2.0 μm pore size) to contain the synthesized

calcite crystals (60.0 ± 0.1 mg). The reactor cell was placed in an oven with the temperature set at 60 ^{o}C. A collection beaker covered with paraffin film was placed outside the oven to sample the output solution for analysis.

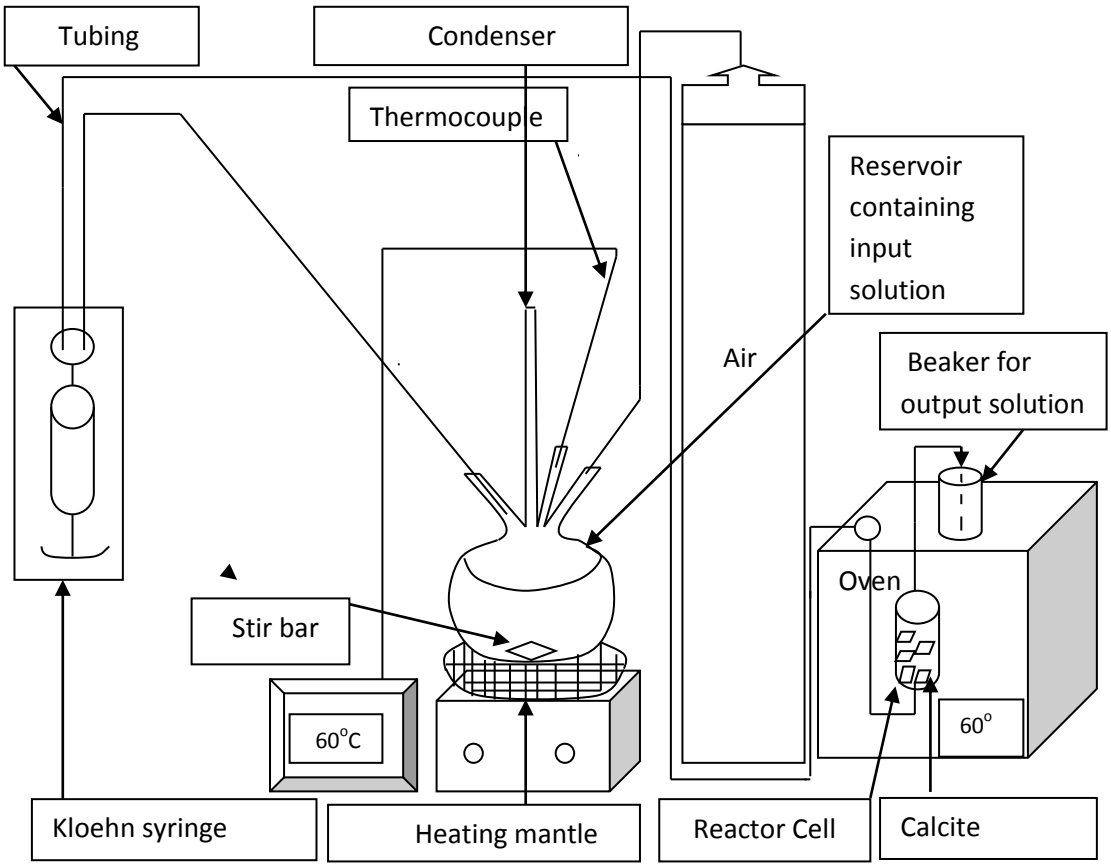

Fig. 2.3: Diagram of the experimental set-up.

2.5 Solution Analysis

To determine total inorganic carbon (i.e., total carbonate), pH and alkalinity determinations were performed (at room temperature) by using a volumetric pipette to extract 25.00 ± 0.05 mL of the output solution from a collection beaker for titrimetric analysis. Alkalinity titrations were performed using 1.00×10^{-2} M HCl which was

prepared from 0.0995 - 0.1005 M HCl standard solution and phenolphthalein and methyl red indicators to obtain carbonate and bicarbonate alkalinity for both the input and output solutions. In carrying out the titrimetric analysis, 25.00 mL of the input solution sample was placed in a 150 mL erlenmeyer flask and 2-3 drops of phenolphthalein added. The mixture was placed on a stir plate and a magnetic stir bar placed into the flask to ensure uniform stirring of the mixture. A 50 mL burette which had been rinsed with deionized water was also mounted on a retort stand. Further rinsing was done using 1.00×10^{-2} M HCl. It was then filled with some of the 1.00×10^{-2} M HCl to reach the 50.00 ± 0.05 mL mark. The 1.00×10^{-2} M HCl was then released into the flask dropwise while stirring until the phenolphthalein endpoint was observed. The new volume of HCl in the burette was then recorded. 2-3 drops of methyl orange was then added to the solution in the flask and after ensuring that the mixture had been uniformly mixed, the acid was again released dropwise into the mixture until the methyl orange endpoint was achieved. The new volume of acid in the burette was recorded. Knowing the initial and final volume of HCl added as well as the volume of input sample used, the concentration of carbonate was obtained. For example, an initial volume of 32.00 ± 0.05 mL was recorded as the volume of HCl and after adding 2-3 drops of phenolphthalein to the input sampled solution and titration, a final volume of 32.05 ± 0.05 mL. The final volume (32.05 ± 0.05 mL) served as the initial volume for further titration using methyl orange as an indicator after which a final volume of 36.05 ± 0.05 mL was recorded. The total inorganic carbon concentration was then obtained as shown in the example below where the volume of HCl used is the volume at the methyl orange endpoint (4.00×10^{-3} L) The same procedure

was employed in determining the total inorganic carbon ($[CO_3^{2-}]_{total} = [CO_3^{2-}] + [HCO_3^-] + [H_2CO_3]$) concentration in the sampled output solution.

$$n\ (HCl) = C_{HCl} \times V_{HCl}$$

$$= 0.01\ mol/L \times 4.00 \times 10^{-3}\ L$$

$$= 4 \times 10^{-5}\ mol$$

$$[CO_3^{2-}]_{total} = \frac{4 \times 10^{-5} mol}{25 \times 10^{-3} L}$$

$$= 1.6 \times 10^{-3}\ mol/L$$

Since the titration does not give $[H_2CO_3]$, it is an approximation.

Analysis for calcium in solutions was performed using Inductively Coupled Plasma Emission Spectroscopy (ICP-ES, Varian 710). Calcium standards of concentrations 5 ppb, 10 ppb, 50 ppb and 100 ppb were prepared from 1000 ppm calcium stock solution and deionized water. These standards were used to generate calibration curves. 1.00 mL of the sampled output and input solutions were taken using a volumetric pipette and diluted to 100.0 mL in volumetric flask using deionized water. The samples were placed in culture tubes and taken to the ICP for analysis. In carrying out the analysis, a sequence was set up based on the number of samples needed to be analyzed and after every 10 samples; the standards were run to test the validity of the calibration. The sequence was set such that triplicate analysis of each sample was obtained for 3 min. The feed tube was rinsed with deionized water in between samples. Based on the linear calibration curve data and the dilution factor used for the samples, calcium concentrations were obtained and a 2 % RSD was recorded.

2.6 Data Analysis

To determine the dissolution rate, Ca^{2+} concentrations from the ICP determinations were used from both the input and output solutions. Using the change in Ca^{2+} concentration from the reactor input to the output, the rate of dissolution was calculated according to the following equation:

$$R(\text{mol cm}^{-2}\text{s}^{-1}) = \frac{Q([Ca^{2+}]_{output} - [Ca^{2+}]_{input})}{A_{total}} \quad (5)$$

where $[Ca^{2+}]_{output}$ and $[Ca^{2+}]_{input}$ are the calcium ion molarities of the output and input solutions, and Q and A_{total} are the flow rate in L/s and the calcite surface area in cm^2, respectively. Using a simple 3-parameter exponential function;

$$R = A + Be^{-t/\tau} \quad (6)$$

where A is the dissolution rate, or so-called "steady rate", in the limit of large t/τ, A + B is the initial rate (t = 0) of dissolution, and τ is the decay (or relaxation) time of the dissolution transient. Curve fitting with weighted standard deviation was accomplished in Igor Pro.

2.7 Etching

The tubing connecting the input solution to the reactor was replaced with new tubing that had been rinsed with deionized water and 0.010 M HCl. One end of the tubing was connected to the reactor cell (in the oven) and the other placed in a 100 mL flask that contained 100 mL of 0.010 M HCl. The flask was covered with paraffin so as to prevent

contamination of the acid with impurities. The opposite opening of the reactor cell also had newly rinsed tubing connecting it to the outside of the oven into a waste collection beaker. Crystals were etched by flowing the 0.010 M HCl through the reactor cell for varying lengths of time (Table 7.1, runs 5-11). The 0-min etch run differs from the un-etched experiment in that in the former, all the experimental steps used to etch the crystals were performed with the exception of the introduction of HCl into the cell. Crystals were etched with 0.010 M HCl for varying lengths of time. Following etching, different undersaturated solutions were run through the reactor cell for 5-8 days. The same procedures employed in sampling the output solution, analysis and dissolution rate determinations as before were used for each run.

Chapter 3

Results

3.1 Influence of saturation state on dissolution kinetics

The effect of solution saturation state on the time-dependent dissolution rates for the synthetic calcite were investigated using five experimental runs with Ω = 0.12, 0.15, 0.25, 0.32 and 0.56. Fig. 3.1 shows a graph of the dissolution rates measured as a function of time. In all experiments, the dissolution rate decreased exponentially with time and in most experiments, the rate approached a nearly constant value after approximately 100 h of reaction. From Fig. 3.1, the initial rates of dissolution as well as the long-term "steady" rates increased with decreasing solute concentration (decreasing Ω). The fitting parameters for the experiments in Fig. 3.1 are summarized in Table 7.1. Fig. 3.2 shows a linear relationship between initial dissolution rate (A + B) and Ω_{inlet}, where a decreasing initial dissolution rate is reflected by increasing solution saturation state as expected from the general kinetic dissolution rate equation, Rate = $k(1- \Omega)^n$, where n = 1, empirically describing many mineral dissolution reactions (Morse et al, 2007). In Fig. 3.3, the steady rate (A), shown as a function of Ω_{inlet}, indicates that the steady rate decreases as the solution saturation state increases towards equilibrium. However, the steady dissolution rate appeared to be nearly independent of Ω_{inlet} in comparing experiments with Ω_{inlet} = 0.32 and Ω_{inlet} = 0.56 making the steady dissolution rates indistinguishable at the closest-to-equilibrium conditions.

Fig. 3.4 shows the saturation state dependence of the decay time for the five experiments described above. The decay time, τ, for the 3 most undersaturated conditions did not appear to be significantly influenced by the saturation state. However,

with an input solution of Ω_{inlet} = 0.56, the rate decay was considerably longer in comparison. A plot of the logarithm of rate vs. time (Run 5), shown as an inset in Fig. 3.1, reveals that the dissolution rate continued to decrease through the end of the 150 h run duration. In addition, due to the lack of a complete dissolution transient, the uncertainty associated with τ was considerably larger in comparison to the uncertainties from the other four experiments.

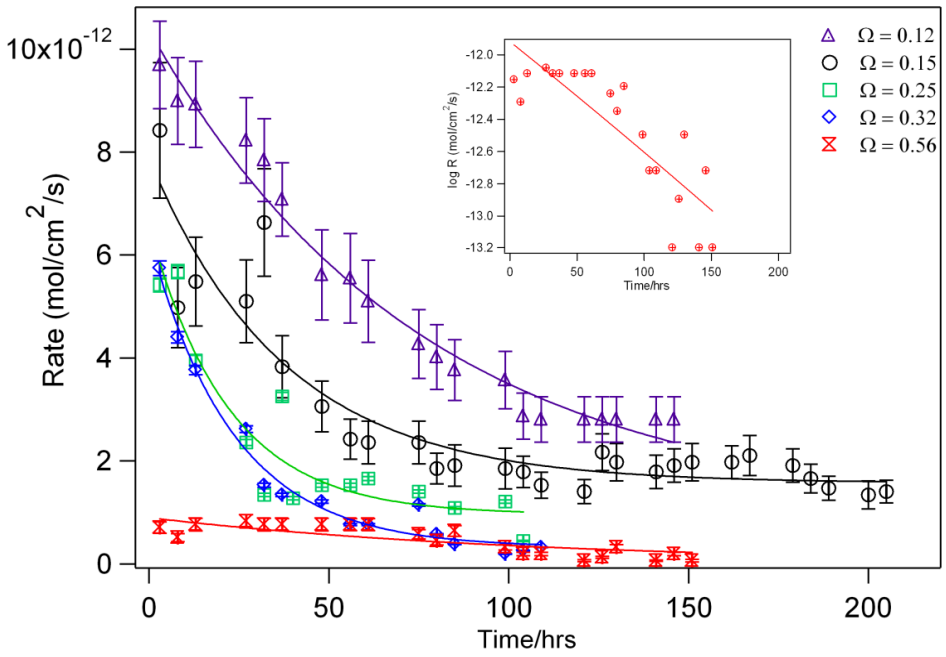

Fig. 3.1: Dissolution rate of calcite versus time at different inlet fluid saturation states Ω_{inlet}.

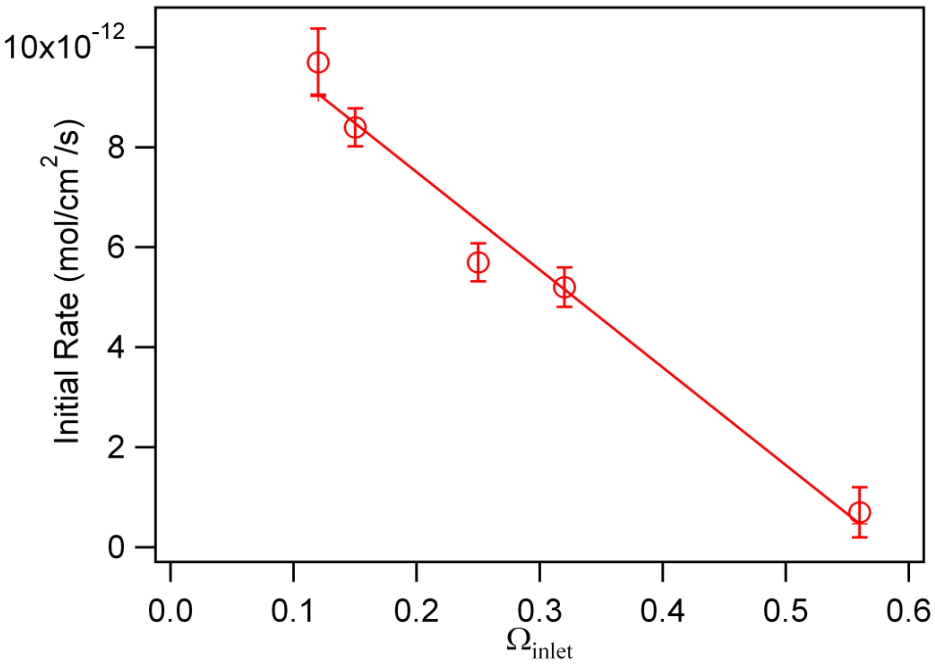

Fig. 3.2: Initial dissolution rate as a function of Ω_{inlet}

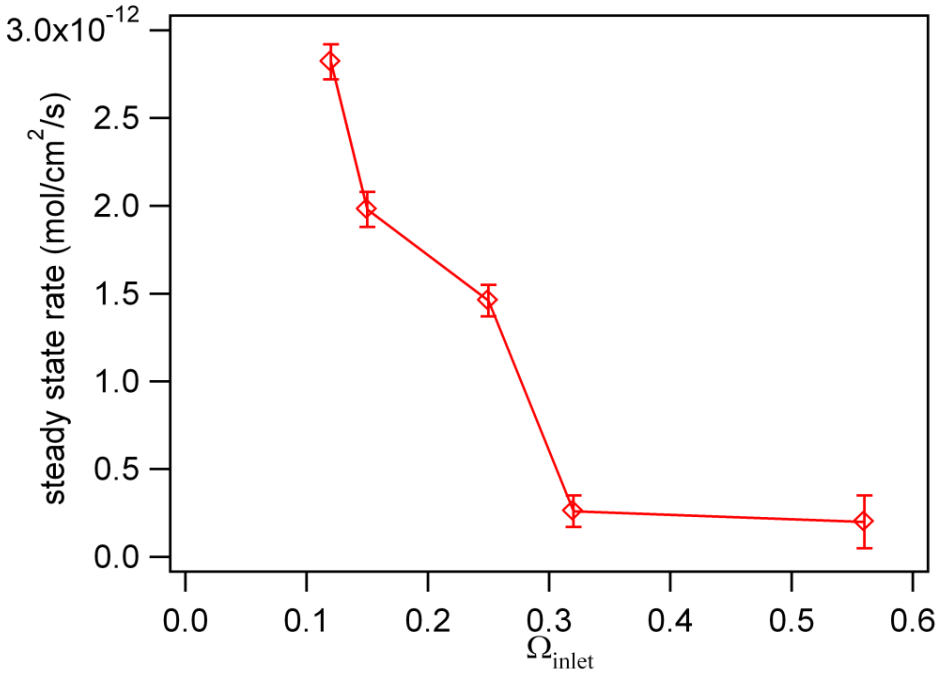

Fig. 3.3: The influence of saturation state on the steady dissolution rate

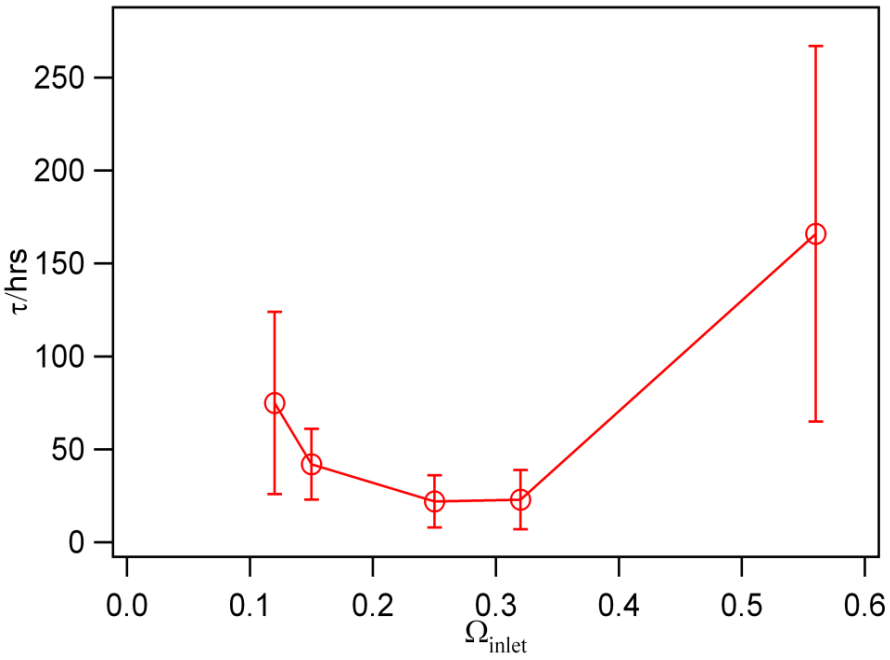

Fig. 3.4: Determining the influence of saturation state, Ω_{inlet} on relaxation time, τ.

3.2 Influence of etching on dissolution kinetics

In Fig. 3.5, the dissolution transients (in Ω = 0.56) for etch times of 0, 10 and 100 minutes along with the un-etched experiment reveal that the duration of the HCl etch has a positive influence on the initial rate of dissolution. In the 0 minute etch run (control experiment), the dissolution rates are approximately the same as the steady dissolution rate for the un-etched and etched runs (i.e. transient rates are not observed for the zero minute etching). The observations in Fig 3.5 are summarized in Fig 3.6 showing that the initial dissolution rates increased with etch duration.

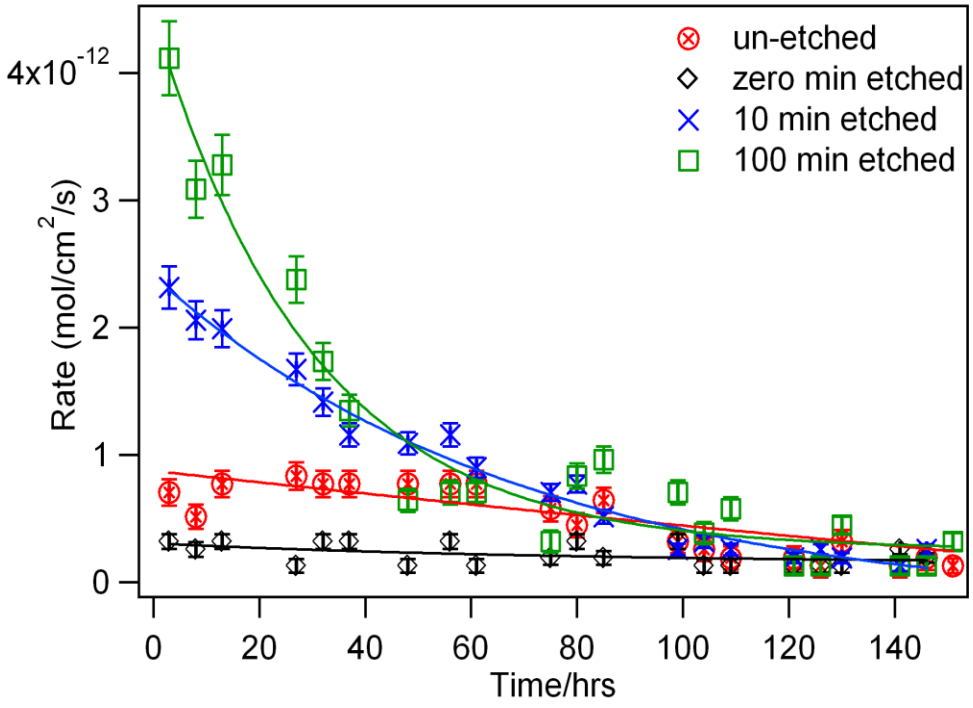

Fig. 3.5: Dissolution rate of calcite at various etch periods at Ω_{inlet} = 0.56

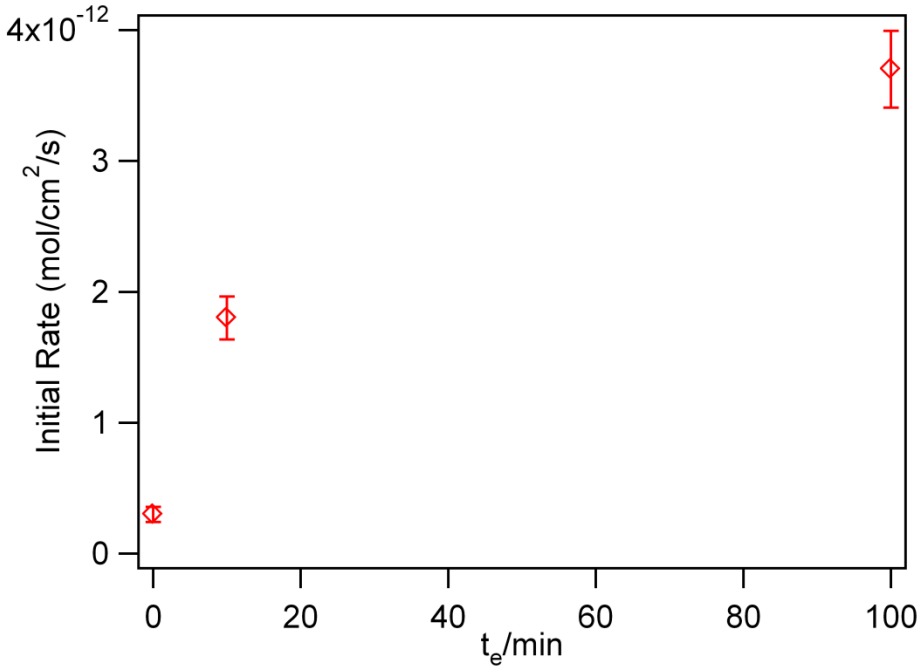

Fig. 3.6: The effect of etch duration on initial dissolution rate at Ω_{inlet} = 0.56.

3.3 Effect of flow rate on dissolution rates

Although the residence time of the FTR in this work was very small (~ 1 min) in comparison to the observed system decay times, the experimental flow rate was varied (3.4 mL/hr and 6.8 mL/hr) to test for possible influence from the rate of mass transport. Two sets of calcite samples of mean size 360 μm were weighed (60.0 mg each) and placed in the reactor cell for two separate experimental runs. The first run was carried out using a flow rate of 3.4 ml/hr and the second 6.8 ml/hr. Both runs were carried out in solutions of the same saturation states (Ω = 0.12) under the same time duration. The dissolution trends observed in the two runs (Fig 3.7) from non-steady state to steady state were indistinguishable and the τ values obtained were approximately the same (Table 7.1).

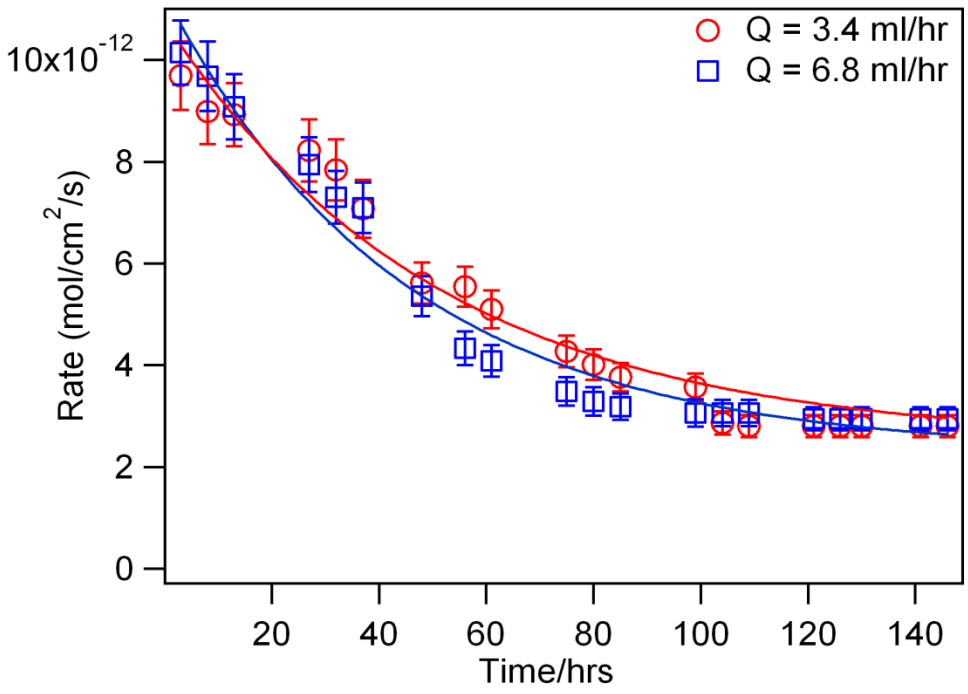

Fig. 3.7: Flow rate influence on calcite dissolution rates with Ω_{inlet} = 0.12

3.4 Crystal size influence on dissolution rate

Using solutions of the same saturation state (Ω = 0.15), two separate experimental runs were carried out on two set of crystals of different sizes (160 µm and 360 µm) at a flow rate of 3.4 ml/hr. Comparing the dissolution rate curves (Fig. 3.8), the relaxation times were similar and the steady dissolution rates appeared to be larger for the smaller crystal size. The differences in the steady dissolution rates is likely due to relatively large uncertainties in the mineral surface areas as determined by the geometric approximations described above.

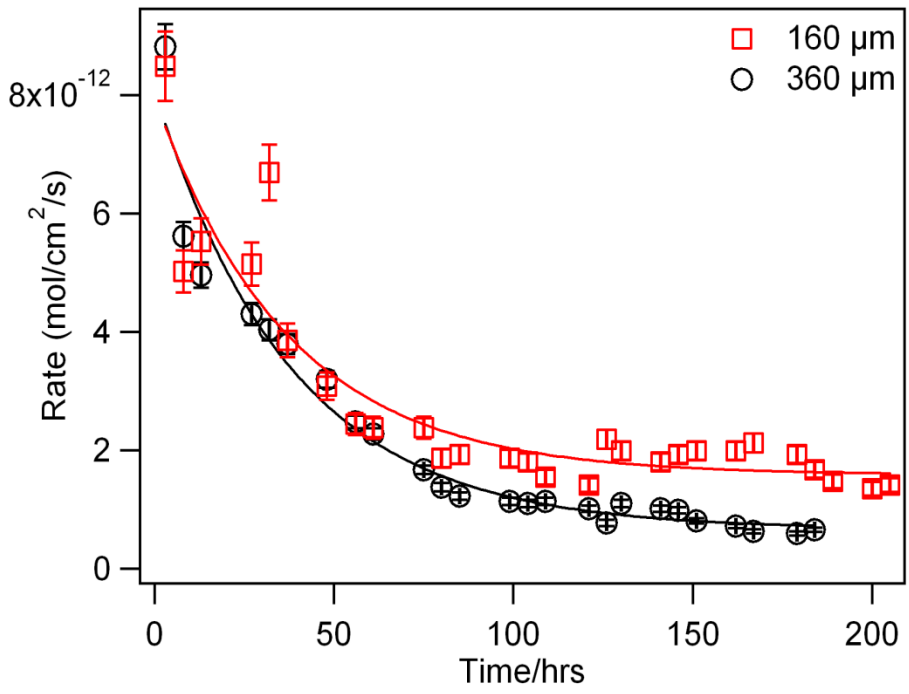

Fig. 3.8: Effect of mean crystal size on dissolution rates

3.5 Topographic comparison of pre- and post- reacted crystal

To enhance our understanding of the morphological changes taking place on the crystal surface during dissolution, AFM images (15 µm × 15 µm) of the reacted (Ω = 0.12, t = 146 h) and un-reacted crystals were taken and compared (Fig. 3.9). A more quantitative comparison of the images is provided through profile data (height vs. lateral position) for a single scan line in each of the two images in Fig. 3.9 as well as pore-size analysis of the crystal before and after reaction in Fig 3.10.

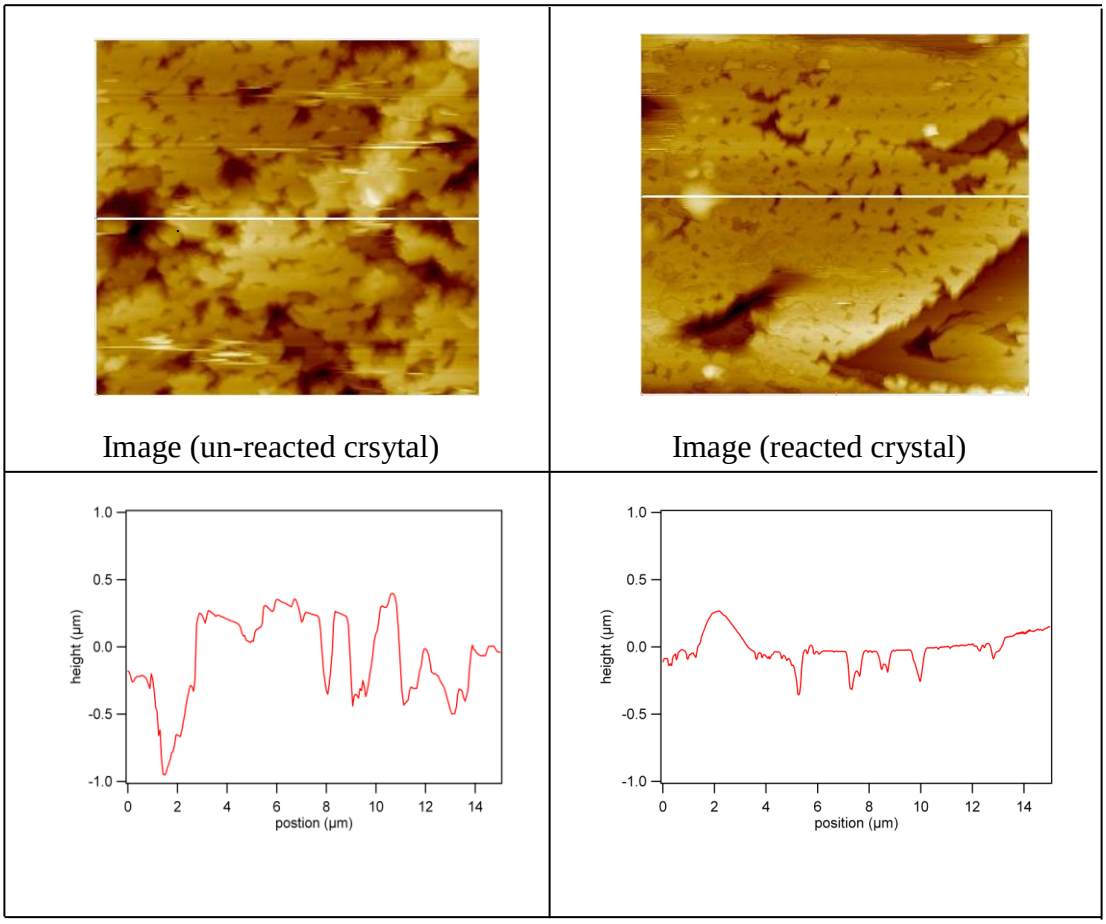

Fig. 3.9: AFM surface topographic images of un-reacted calcite and reacted calcite crystal ($10\bar{1}4$) of sizes 15 µm × 15 µm and their corresponding vertical surface relief plots.

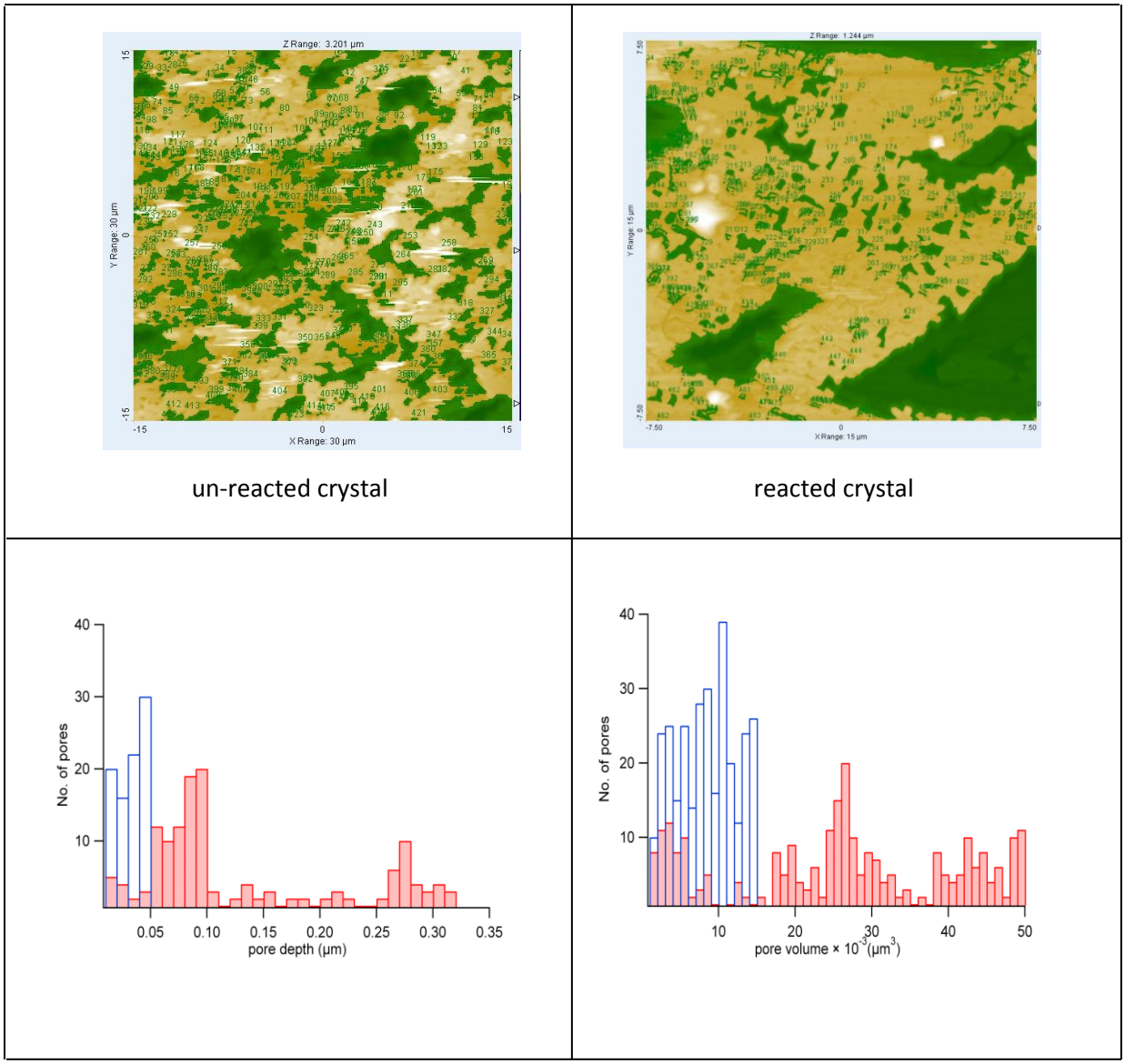

Fig. 3.10: Analysis of the pre- and post- calcite crystal with their respective histograms of the pore volume and pore mean depth using Scanning Probe Image Processor (SPIP). In both histograms the red and blue bars represent pre- and post- reacted calcite, respectively.

The surface relief plot for both the un-reacted and reacted crystal indicated the presence of varied pore sizes and depths (Fig. 3.9) with the pre- analyzed crystal being characterized by deeper pores.

Using Scanning Probe Image Processor (SPIP), the pore volumes and areas were obtained and in determining the mean pore depth, the total pore volume was divided by total pore area. However, the very large pores were excluded in the calculation due to the fact that they oftentimes were not captured within the image area. Fig. 3.10 shows histograms of the pore size analysis of both the un-reacted surface and the reacted surface. For the unreacted surface, an average pore volume and mean depth of ~ 26×10^{-3} μm^3 and ~ 90×10^{-3} μm were obtained respectively whereas the reacted surface showed an average pore volume and mean depth of ~ 9.9×10^{-3} μm^3 and ~ 37×10^{-3} μm, respectively, suggesting that the pores had decreased in both volume and depth after dissolution. The amount of material that had dissolved from the dissolution run and the amount dissolved after the SPIP analysis of the AFM images were determined as well.

Considering the dissolution run (Fig. 3.1, $\Omega = 0.12$), the initial amount (moles) of material before the run was known from the mass and molar mass of calcite that had been placed in the reactor. In determining the amount of calcite dissolved after the experimental run, a plot of dissolution rate as a function of time was obtained (Fig. 3.1, $\Omega = 0.12$) and the area (moles of material) under the graph obtained by integration. Knowing the amount of material before and after dissolution, the amount of calcite dissolved was obtained. On the other hand, in calculating the amount of material dissolved from the AFM analysis (using SPIP), layer-by-layer dissolution is assumed to occur resulting in the pits appearing shallower in time. As fluid flows on the surface and within the pits, the diffusion fields in the shallow and deep pits are likely to differ from one another. In the deep pits where the fluid may be relatively stagnant, the solution composition approaches equilibrium ($\Omega \sim 1$) thus impeding dissolution especially at the

bottom of the pits in our near equilibrium environment hence dissolution may proceed via existing steps on the walls that are relatively close to the topmost terraces where $\Omega < 1$ resulting in lateral removal of material as the steps retreat. Using the model of dissolution in Fig. 7.17, the volume of material dissolved (AFM/SPIP analysis) was first determined by multiplying the approximate mean depth (i.e. change in mean depth of the pre- and post- sample) by the total surface area of calcite placed in the reactor, A_{total} obtained in equation (3). Using the volume dissolved and the density of calcite, the mass of material and subsequently the amount dissolved was calculated. From the pore analysis data, $\sim 5 \times 10^{-7}$ mol of material had dissolved but the dissolution rate data from the flow through reactor ($\Omega = 0.12$, un-etched) reveals $\sim 1 \times 10^{-5}$ mol of material dissolved from the calcite sample in the reactor with an initial amount of 6×10^{-4} mol indicating a significant differences in the two models of dissolution.

Chapter 4

Discussion

In a dissolution model earlier proposed by Bose et al. (2008), it was observed that dissolution occurred preferentially at step edges in comparison to the terrace of a mineral. Dissolution in the etch pits (comprised of step edges) occurred via step retreat leading to lateral expansion of the pits as illustrated in Fig. 4.1 where the curved lines indicate the elementary step edges retreating over time and the shaded portions, the pits on the surface of the crystal whose walls are comprised of elementary step edges. According to the authors, longer durations of dissolution resulted in pit-pit overlap suggesting that the pit population and step density decreased over time.

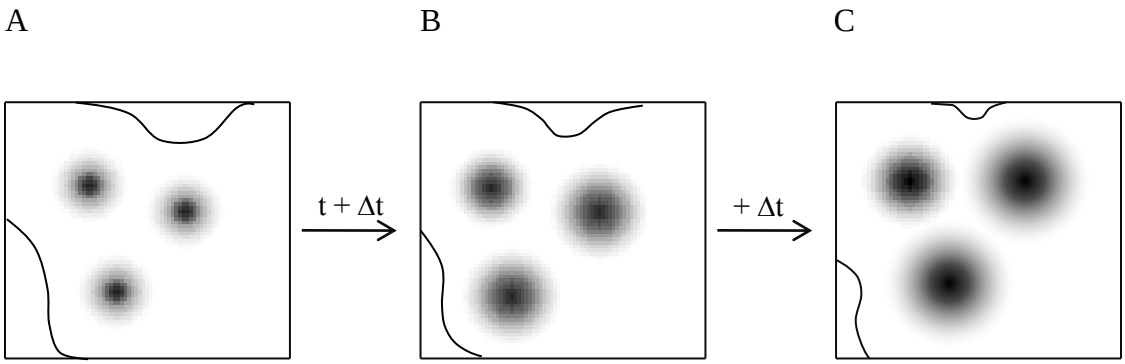

Fig. 4.1: Schematic representation of how the reactive surface sites evolve over time according to Bose model. (A) Shows the surface of the crystal before dissolution where shaded circles represent the pits and the curved lines, step edges. (B) and (C) indicates continuous lateral expansion of pits in the long term.

The topographic relaxation time, τ according to Bose et al. (2008), is a function of pit spacing, c and step speed V_s, $\tau \sim c(2V_s)^{-1}$ but our experimental results do not agree with predictions based on near equilibrium step speeds (~ 1 nm/s) at 60 ^{o}C by AFM (Xu et al, 2010) wherein the step speeds and observed relaxation times above give a predicted pit

spacing of about 100 μm which is much larger than the pit spacing observed in Fig. 3.9. From the Bose model, τ is found to depend on the spacing between pits and the fact that the observed pit spacing differed significantly from prediction indicated that other material characteristics, such as crystal size might influence τ as well. Since the observed τ led to a predicted pit spacing, $c \sim 100$ μm which was about the size of the crystal, (e.g., 300 μm), crystals of smaller sizes (160 μm) were synthesized and dissolution runs performed. However, the observed τ recorded in our experiments (Table 7.1) of different crystal sizes show that τ is not dependent on the size of the crystals. The initial rates were also similar (Fig. 3.8). While the steady dissolution rates are found to be larger for the smaller size crystals, this difference in steady rates is likely to be due to the large uncertainties (i.e. 25 % and 34 % for the smaller and larger size crystals, respectively) in the surface area determination.

Increasing the flow rate by a factor of two did not have any significant influence on the relaxation time and the steady dissolution rate (Fig. 3.7). AFM experiments in the past (Liang and Baer 1997) showed a weak dependence of dissolution rate on fluid flow rate at and above a critical fluid flow rate with the dissolution rate being surface controlled. The lack of flow rate influence on the dissolution rate suggests that the reaction rates were more likely to be surface controlled.

From the dissolution model proposed by Bose et al. (2008), τ should vary inversely with step speeds, which in turn will generally vary linearly with Ω (Xu et al, 2010) but Fig. 3.4 shows an unexpected constancy in τ over a range in Ω_{inlet} and τ becomes difficult to determine as $\Omega \rightarrow 1$. AFM experiments (Xu et al, 2010; Teng, 2004) revealed that at $\Omega \geq 0.30$ etch pit formation does not occur. Therefore, dissolution under these near-

equilibrium conditions would have to proceed through retreat of existing step edges. If etch pit generation is likewise not significant in our near-equilibrium experiments, then the time-dependent dissolution rate should represent the rate of loss of step density as step-step annihilation takes place. As discussed in Bose et al. (2008), the rate of step density loss (i.e., surface smoothing) should be affected by step speeds which in turn are influenced by the saturation state. Our data at saturation states of $\Omega < 0.56$ are contrary to the predicted trend. That is, the closer to equilibrium experiments should have had lower step speeds and therefore longer relaxation times. At $\Omega = 0.25$ and 0.32, nearly the same τ values were obtained but slightly higher τ value was observed at $\Omega = 0.12$-0.15. It is possible that due to the higher undersaturation of the latter, the generation of etch pits was significant and the model developed by Bose et al. (2008) did not consider how etch pit formation would alter the approach to a steady surface morphology. However, when the experimental solution was very close to equilibrium ($\Omega = 0.56$), τ was found to increase, indicating a positive correlation between saturation state and relaxation time, although the uncertainty in τ is large.

Since crystal size variation did not influence τ, we assume that the pit spacing determined from the AFM images is appropriate in the Bose et al. model. The longer τ values observed therefore imply that the measured step speeds, $V_s \sim 1$ nm/s recorded by Xu et al. (2010), do not apply to our study of calcite dissolution. Rather step speeds of ~ 0.01 nm/s would provide a predicted relaxation time closer to our observations. The retreat of steps mainly occurs as solution moves on the crystal surface and within the pits. However, where the solution remains fairly stagnant within pits, local equilibrium is achieved and step speeds may be considerably reduced, limited in speed by the rate of

mass transport (diffusion) out of the pits. Using Fick's first law of diffusion and diffusion coefficient of calcium, $D_{Ca} = 7.6 \times 10^{-6}$ cm^2/s as reported by Sjoberg and Rickard, 1985, for the pore depth ($\Delta x = 53$ nm) determined from SPIP analysis, the diffusion limited rate (5.41×10^{-9} $mol/cm^2/s$) at the closest to equilibrium state ($\Omega_{outlet} = 0.77$, Table 7.2) obtained was 3 orders of magnitude greater than the experimentally determined rate (9.71×10^{-12} $mol/cm^2/s$, $\Omega_{outlet} = 0.77$, Table 7.2) suggesting that diffusion from the pores is not a limiting factor in dissolution of these experiments.

Another factor that may contribute to the longer relaxation time is the influence of impurities. Experiments in the past (Berner, 1967; Weyl, 1967; Harstad and Stipp, 2007; Ruiz Agudo et al, 2009) indicate that trace divalent cations such as Mn^{2+}, Mg^{2+}, and Sr^{2+} that may be substituted for Ca^{2+} in calcite despite high purity materials used in its synthesis (Paquette and Reeder, 1995), are found to pose inhibitory effects on step edge dissolution. Apart from these impurities that may be present in the synthesized crystals, AFM experiments in the past (Xu et al, 2010; Arvidson, 2006) suggests that step pinning by impurities such as Mg^{2+} that attach to step edges can greatly impede the detachment of Ca^{2+} thus inhibiting and decreasing dissolution. Although these impurities may not be permanently substituted, especially in a dissolution process, they can influence the dissolution kinetics.

According to recent AFM experiments by Xu et al. (2010), depending on the concentration of Mg^{2+} impurity and solution undersaturation, pinning of steps may occur. In that study, upon the addition of 10^{-4} molal Mg^{2+}, negligible impurity effects were observed on calcite dissolution under near equilibrium conditions. In the presence of 10^{-3} molal Mg^{2+} at $\Omega < 0.2$, inhibitory effects were not easily observed but at $\Omega \geq 0.2$, step

motion ceased indicating the significant influence of impurities such as Mg^{2+} dissolution rate. Terjesen et al. (1961) also indicated that at very low levels of trace species, strong retarding effects on calcite dissolution of micro molar concentrations of dissolved Sc^{4+} can occur suggesting that even in the presence lower concentration of trace elements, relatively higher step speeds may be observed in an impurity free environment in comparison to impurity induced conditions hence lower dissolution rate and longer τ values may characterize the impurity prone environment.

One manifestation of impurities that is evident in the AFM observations is the profile of the pores, which all appear with steep sidewalls or defects. According to Schott et al. (1989), of all the reactive sites on the calcite mineral, facets (terraces) are the least reactive. Therefore if the pit walls are not comprised of independently dissolving steps but rather facets, then the rate of pit opening becomes far less than the rate of independent step retreat. This implies that pit expansion speed may be significantly lower than the elementary step speed. The prediction inferred from the AFM step speed data by Xu et al. (2010) for the system of particles used may therefore be incorrect due to the difference in the true surface morphology compared with the expected morphology.

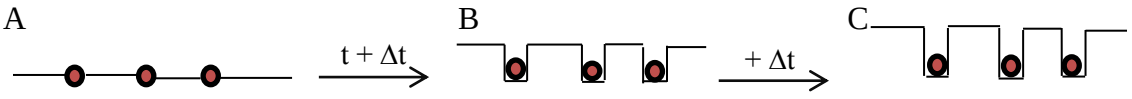

Fig. 4.2: The growth of pits with impurities or point defects on the crystal surface during crystal growth indicating how the pits develop facets rather than step edges. In (A), the shaded circles are the impurities or pre-existing defects bounded by step edges (horizontal lines). (B) shows the development of facets as the pits grow and the growth continues with time as seen in (C).

Etching resulted in larger initial rates (Fig. 3.5). At $\Omega = 0.56$, the initial dissolution rate for the 100 min etch run was 6 times larger than that of the un-etched run. This observation is likely to be as a result of an increase in the number of surface pits as well as deepening of pre-existing pits on the as-prepared calcite crystals (Fig. 3.5). Increased step density is consistent with previous observations (MacInnis and Brantley, 1992) where larger initial rates of dissolution of calcite were observed in a rotating disc experiment after pre-treating calcite sample with 10^{-3} M HCl for 20 min.

Most of the pits that were initially found on the mineral surface appear to have been reduced in surface density after going through a significant amount of dissolution as we observe in the pre- and post-reacted topographic images taken from the AFM (Fig. 3.9) and their respective line profile plots. However, in the SPIP analysis of the AFM images (Fig. 3.10) the amount of material ($\sim 5 \times 10^{-7}$ mol) determined to have dissolved was far less than the amount of material dissolved from the flow-through reactor data ($\sim 1 \times 10^{-5}$ mol). If dissolution were to occur via layer-by-layer removal of monolayer steps according to a proposed model (Fig. 7.17) then more material (~ 20× from a pit depth of ~ 0.09 μm) needed to dissolve to account for the material dissolved ($\sim 1 \times 10^{-5}$ mol) based on chemical analysis from the flow-through reactor. To have more material dissolved ($\sim 1 \times 10^{-5}$ mol) as is found to be the case in the flow-through reactor, then a model of dissolution such as the one described by Bose et al. (2008) is more likely.

Chapter 5

Conclusion

The rate of dissolution of calcite undergoes exponential decay with time (Fig. 3.1), approaching a limiting or steady rate in the long term. A linear proportionality existing between the initial dissolution rate and Ω_{inlet} (Fig. 3.2) agrees with earlier experiments (Sjoberg and Rickard, 1983) in that the rate detachment of lattice ions from the mineral surface is enhanced as the solution undersaturation increases. The saturation state influence on steady dissolution rate (Fig. 3.3) also shows a linear relationship except in the range $\Omega = 0.32 - 0.56$ when the steady rate follows a weaker dependence on Ω. Since transient and initial rates decrease as near equilibrium conditions are approached as seen in this study (Fig. 3.1) and other studies (Gledhill and Morse 2004) where dissolution is assumed to occur mainly by step retreat (Teng et al, 2004), the steady rates are also likely to decrease as solution undersaturation decreases as seen in Fig. 3.3 such that in short term experimental runs such as this study, steady rates of relatively near equilibrium solution saturation states ($\Omega = 0.32 - 0.56$) may be indistinguishable from one another.

The flow through reactor data for calcite presented in this study confirms earlier observations (Berner and Morse 1974) reported where the dissolution trend is characterized by higher initial and transient rates. The dissolution decay occurs after most of the reactive sites such as kinks, corners and step edges that define surface etch pits have dissolved. Sample history also influences the dissolution trend as was earlier investigated by Arvidson and Luttge (2010) where surfaces with more etch pits (pre-treated surfaces) are found to have higher non-steady state rates compared to surfaces

with few or no dislocations. A similar transient dissolution rate trend was found in our etch runs where pre-etched calcite samples recorded larger transient rates as etch duration increases.

The kinetic data presented here also reveal that etch pit formation influences the approach to steady surface morphology and τ may not necessarily depend on Ω unless at very near equilibrium conditions ($\Omega > 0.32$) where etch pit formation is highly disfavored. The topographic relaxation, τ, however poses significant challenge especially at very close to equilibrium states and appears to vary from one study to the other. Gledhill, 2004, indicated ~ 6 h relaxation time in the dissolution of calcite. In this study we predicted a relaxation time of ~30 h for calcite and even higher at $\Omega = 0.56$ wherein factors such as dissolution diffusion field differences in the pits and pores and the influence of impurities are thought to be the cause of the longer τ values. The accurate prediction of τ therefore requires additional experiments where etch pit characterization and the inhibitory effects of various impurities will provide detail information towards the prediction of τ to aid in the development of consistent dissolution models linking laboratory experiments to geologic fields towards effective CO_2 sequestration.

REFERENCES

Alkattan M., Oelkers E. H., Dandur and J. L., and Schott J. (2002). An experimental study of calcite dissolution rates at acidic conditions and 25^{o} C in the presence of $NaPO_3$ and $MgCl_2$. *Chemical Geology*, **190**, 291-302.

Arvidson S. R. and Luttge A. (2010) Mineral dissolution kinetics as a function of distance from equilibrium – New experimental results, *Chemical Geology*, **269**, 79-88.

Arvidson S. R., Collier, M., Davis K. J., Vinson M. D., Amonette E. J., and Luttge, A. (2006). Magnesium inhibition of calcite dissolution kinetics. *Geochimica et Cosmochimica Acta*, **70**, 583-594.

Bachu S. (2000) Sequestration of CO_2 in Geological Media: Criteria and Approach for Site Selection in Response to Climate Change. *Energy Conversion and Management*, **41**, 953-970.

Berner R.A. (1975). The role of magnesium in the crystal growth of calcite and aragonite from Sea water. *Geochimica et Cosmochimica Acta*, **75**.

Berner R. A. (1967). Comparative dissolution characteristics of carbonate minerals in the presence and absence aqueous magnesium ion. *American Journal of Science*, **265**, 45-70.

Berner R. A. and Morse J. W. (1974). Dissolution kinetics of calcium carbonate in sea water: IV. Theory of calcite dissolution. *American Journal of Science*, **274**, 108-134.

Bose S., Hu X., and Higgins, S. R. (2008). Dissolution kinetics and topographic relaxation on celestite (001) surfaces: the effect of solution saturation state studied using Atomic Force Microscopy. *Geochimica et Cosmochimica Acta*, **72**, 759-770.

Brantley S. L., and Koepenic, K. (1995). Measured carbon dioxide emissions from Oldoinyo Lengai and the skewed distribution of passive volcanic fluxes. *Geology*, **23**, 933-936.

Brunauer S., Emmet P. H., Teller E. (1938). Absorption of gases and multimolecular layers. *Journal of the American Chemical Society*, **60**, 309-319.

Burton W. K., Cabrera N., and Frank F. C. (1951). The growth of crystals and the equilibrium structure of their surfaces. Philos. *Trans. R Soc. Lond A*, **243**, 299-358.

Busenberg E., and Plummer L. N. (1986). A comparative study of the dissolution and precipitation kinetics of calcite and aragonite. In: Mumton, F.A. (Ed.), Studies in Diagenesis. U. S. Geological Survey Bulletin. 139-168.

Cabrera N. and Levine M. M. (1956). On the dislocation theory of evaporation of crystals. *Philosophical Magazine*, **1**, 450-458.

Cabrera N., Levine M. M., and Plaskett J. S. (1954). Hollow dislocations and etch pits. *Physical Review*, **96**, 1153.

Caldeira K., and Rau, H. G. (2000). Accelerating carbon dissolution to sequester carbon dioxide in the ocean: Geochemical implications. *Geophysical Research Letters*, **27**, 225-228.

Chou L., Garrels M. R., and Wollast R. (1989). Comparative study of the kinetics and mechanisms of dissolution of carbonate minerals. *Chemical Geology*, **78**, 269-282.

Dreybrodt W. (1981). Kinetics of dissolution of calcite and its application to kartstification. *Chemical Geology*, **31**, 245-269.

Friedman, G. M. (1964). Early diagenesis and lithification in carbon sediments. *Journal Sediment Petroleum*, **34**, 777-813.

Giudici G. D. (2002). Surface control vs. diffusion control during calcite dissolution: dependence of step edge upon solution pH. *American Minerology*, **87**, 1279-1285.

Gledhill D. K. and Morse J. W. (2004). Dissolution kinetics of calcite in NaCl-$CaCl_2$-$MgCl_2$ Brines at 25 ^oC and 1 bar pCO_2. *Aquatic Geochemistry*, **10**, 171-190.

Gutjar A., Dabringhaus H., and Lacmann, R. (1996a) Studies of the growth and dissolution kinetics of the $CaCO_3$ polymorphs calcite and aragonite: I. Growth and dissolution rates in water. *Journal Crystal Growth*, **158**, 296-309.

Harstad A. O. and Stipp S. L. S. (2007). Calcite dissolution: effects of trace cations naturally present in Iceland spar calcites. *Geochimica et Cosmochimica Acta*, **71**, 56-70.

Hodson, E. M. (2006). Does reactive surface area depend on grain size? Results from pH 3, 25 ^oC far-from-equilibrium flow-through dissolution experiments on anorthite and biotite. *Geochimica et Cosmochimica Acta*, **70**, 1655-1667.

Lasaga, A. C. and Luttge A. (2001). Variation of dissolution rate based on a dissolution stepwave model. *Science*, **291**, 2400-2400.

Lea S. A., Amonette E. J., Baer D. R., Liang Y., and Colton G. N. (2001) Microscopic effects of carbonate, manganese and strontium ions on calcite dissolution *Geochimica et Cosmochimica Acta*, **65**, 369-367.

Liang Y., Baer D. R., McCoy M. J., Amonette E. J., and Lafemina J. P. (1996). Dissolution kinetics at the calcite-water interface. *Geochimica et Cosmochimica Acta*, **60**, 4883-4887.

Liang Y. and Baer D. R. (1997). Anisotropic dissolution at the $CaCO_3$ ($10\bar{1}$ 4)-water interface. *Surface Science*, **373**, 275-278.

MacInnis I. N. and Brantley S. L. (1991). The role of dislocations and surface morphology in calcite dissolution. *Geochimica et Cosmochimica Acta*, **56**, 1113-1126.

Morse J. W. and Arvidson R. S. (2002). The dissolution kinetics of major sedimentary carbonate minerals. *Earth Science Reviews*, **58**, 51-84.

Morse J. W., Arvidson S. R., and Luttge A. (2007). Calcium carbonate formation and dissolution. *Chemical Reviews*, **107**, 342-381.

Morse J. W. and Mackenzie F. T. (1990). Geochemistry of Sedimentary Carbonates. *Elsevier Science*.

Murray, J., and Renard, A. F. Report on deep- sea deposits based on specimens collected during the voyage of H.M.S. Challenger in the years 1872-1876. Report on the Scientific Results of the Voyage of HMS. London (Longmans), 1891.

Oelkers E. H. and Schott J. (2005). Geochemical aspects of CO_2 sequestration. *Chemical Geology*, **217**, 183-186.

Patel C. R., Boe J. R., and Atkinson G. (1973). The CO_2-water system. I. Study of the slower hydration-dehydration step. *Journal of Solution Chemistry*, **2**, 357-372

Paquette J. and Reeder R. J. (1995). Relationship between surface structure, growth and trace element incorporation in calcite. *Geochimica et Cosmochimica Acta*, **59**, 735-749.

Plummer L. N. and Wigley T. M. L. (1976) The dissolution of calcite in CO_2 – saturated solutions at 25^oC and 1 atmosphere total pressure. *Geochimica et Cosmochimica Acta*, **40**, 191-202.

Pokrovsky O. S., Golublev S. V., Scott J., and Castillo A. (2009). Calcite, dolomite and Magnesite dissolution kinetics at acid to circumneutral pH, 25

to 150 ^{o}C and 1 to 55 atm pCO_2: New constraints on CO_2 sequestration in sedimentary basins. *Chemical Geology*, 2009, **260**, 317-329.

Ruiz-Agudo E., Putnis C. V., Jimenez-Lopez C., and Rodriguez-Navarro C. (2009). An atomic force microscopy study of calcite dissolution in saline solutions: the role of magnesium ions. *Geochimica et Cosmochimica Acta*, **73**, 3201-3217.

Schott J., Brantley S. L., Crerar D., Guy C., Borcisk M., and William C. (1989). Dissolution kinetics of strained calcite. *Geochimica et Cosmochimica Acta*, **53**, 373-383.

Shiraki R., Rock P. A., and Casey W. H. (2000). Dissolution kinetics of calcite in 0.1 M NaCl solution at room temperature: An atomic force microscopy (AFM) study. *Aquatic Geochemistry*, **6**, 87-108.

Sjoberg E. L. and Rickard D. T. (1983). The influence of experimental design on the rate of calcite dissolution. *Geochimica et Cosmochimica Acta*, **47**, 2281-2286.

Sjoberg E. L. and Rickard D. T. (1983). Mixed kinetic control of calcite dissolution rate. *American Journal Science*, **283**, 815-830.

Sjoberg E. L. and Rickard D. T. (1984). Calcite dissolution kinetics: Surface speciation and the origin of variable pH dependence. *Chemical Geology*, **42**, 119-136.

Sjoberg E. L. and Rickard D. T. (1985). The effect of added dissolved calcium on calcite dissolution kinetics in aqueous solution at 25 ^{o}C. *Chemical Geology*, **49**, 405-413.

Skoog A. D., West M. D., and Holler F. J. (1988) *Fundamentals of Analytical Chemistry*, 5th Ed, Saunders College Publishing, New York, 41-44.

Teng H. H. (2004). Controls of saturation state on tech pit formation during calcite dissolution. *Geochimica et Cosmochimica Acta*, **68**, 253-262.

Terjesen S. G., Erga O., Thorsen G., and Ve A. (1961). Phase boundary processes as rate determining steps in reactions between solids and liquids: The inhibitory action of metal ions on the formation of calcium bicarbonate by the reaction of calcium with aqueous carbon dioxide. *Chemical Engineering Science*, **74**, 277-288.

Xu M., Hu X., Knauss K. G., and Higgins S. R. (2010). Dissolution kinetics of calcite at 50 to 70 ^{o}C: An atomic force microscopic study under near equilibrium conditions. *Geochimica et Cosmochimica Acta*, **40**, 191-202.

Xu M. and Higgins S. R. (2010). Effects of magnesium ions on near-equlibruim calcite dissolution: Step kinetics and morphology. *Geochimica et Cosmochimica Acta*.

Weyl P. K. (1958). The solution kinetics of calcite. *Journal Geology*, **66**, 163-176

Wissbrun F. K., French M. D., Patterson A. (1954). The true ionization constant of carbonic acid in aqueous solution from 5 to 45 ^{o}C. *Journal of Physical Chemistry*, **58**, 693-695.

Appendix

Table 7.1: Experimentally determined rate and relaxation time, τ at various saturation states, Ω

Run #	Etched time (min)	Ω	Measured pH	Initial Rate (mol/cm^2/s) $\times 10^{-12}$	τ	Limiting rate (mol/cm^2/s) $\times 10^{-12}$
1-0	-	0.12	8.12	9.7 ± 0.5	75 ± 49	2.82 ± 0.03
1-1	-	0.12	8.12	10.1 ± 0.4	68 ± 30	3.19 ± 0.04
2-0	-	0.15	8.14	8.4 ± 0.3	42 ± 19	1.98 ± 0.05
2-1	-	0.15	8.14	8.6 ± 0.5	43 ± 32	0.63 ± 0.03
3	-	0.25	8.18	5.7 ± 0.2	22 ± 14	1.56 ± 0.04
4	-	0.32	8.20	5.2 ± 0.1	23 ± 16	0.26 ± 0.03
5	-	0.56	8.24	0.7 ± 0.1	166±101	0.03 ± 0.01
6	0	0.56	8.24	0.3 ± 0.1	82 ± 52	0.03 ± 0.01
7	10	0.56	8.22	1.8 ± 0.1	105± 54	0.02 ± 0.01
8	100	0.56	8.23	3.7 ± 0.2	120± 58	0.01 ± 0.01
9	1	0.32	8.19	5.8 ± 0.1	28 ± 17	0.44 ± 0.02
10	100	0.32	8.18	8.4 ± 0.2	56 ± 35	0.02 ± 0.01
11	10	0.15	8.14	8.4 ± 0.2	65 ± 44	1.38 ± 0.03

Runs 1-0 and 1-1 represents experiments with flow rates 3.4 mL/hr and 6.8 mL/hr respectively whiles runs 2-0 and 2-1 represents experiments with crystal sizes 360 μm and 160 μm respectively. In run 6, τ was determined after constraining the experimental data from 56 – 151 hrs.

Table 7.2: Experimental results for solution saturation state, Ω_{inlet} = 0.12 of pH = 8.12 using 360 µm (un-etched) crystals at a flow rate of 3.4mL/hr.

Time hr	$[Ca^{2+}]_{inlet}$ Ppm	$[Ca^{2+}]_{outlet}$ ppm	$\Delta[Ca^{2+}]$ Ppm	Expt. Outlet pH at 25 ºC	Calc. outlet pH at 25 ºC	Ω_{outlet} at 60 ºC	$[CO_3^{2-}]_{outlet}$ Molar	Rate mol/cm^2/s	Rate uncertainty
3	0.42	1.93	1.51	8.15	8.41	0.77	1.60E-03	9.71E-12	6.71E-13
8	0.43	1.87	1.44	8.15	8.41	0.76	1.60E-03	9.26E-12	6.41E-13
13	0.42	1.82	1.40	8.15	8.41	0.74	1.60E-03	9.00E-12	6.24E-13
27	0.43	1.81	1.38	8.14	8.41	0.74	1.60E-03	8.87E-12	6.15E-13
32	0.41	1.75	1.34	8.14	8.38	0.62	1.50E-03	8.62E-12	5.98E-13
37	0.41	1.69	1.28	8.14	8.38	0.56	1.50E-03	8.23E-12	5.72E-13
48	0.41	1.29	0.88	8.14	8.38	0.53	1.50E-03	5.66E-12	4.01E-13
56	0.41	1.28	0.87	8.14	8.38	0.52	1.50E-03	5.59E-12	3.97E-13
61	0.41	1.21	0.80	8.14	8.38	0.50	1.50E-03	5.14E-12	3.68E-13
75	0.41	1.08	0.67	8.14	8.38	0.48	1.50E-03	4.31E-12	3.14E-13
80	0.41	1.04	0.63	8.14	8.38	0.46	1.50E-03	4.05E-12	2.97E-13
85	0.41	1.00	0.59	8.14	8.38	0.45	1.50E-03	3.79E-12	2.80E-13
99	0.42	0.98	0.56	8.14	8.38	0.43	1.50E-03	3.60E-12	2.68E-13
104	0.42	0.87	0.45	8.14	8.38	0.43	1.50E-03	2.89E-12	2.25E-13
109	0.41	0.85	0.44	8.13	8.38	0.41	1.50E-03	2.83E-12	2.21E-13
121	0.39	0.83	0.44	8.13	8.38	0.43	1.50E-03	2.83E-12	2.19E-13
126	0.39	0.83	0.44	8.13	8.38	0.43	1.50E-03	2.83E-12	2.19E-13
130	0.39	0.83	0.44	8.13	8.38	0.41	1.50E-03	2.83E-12	2.19E-13
141	0.39	0.83	0.44	8.13	8.38	0.41	1.50E-03	2.83E-12	2.19E-13
146	0.39	0.83	0.44	8.13	8.38	0.43	1.50E-03	2.83E-12	2.19E-13

Ω_{outlet} represents the computed saturation state of the output sample solution which was obtained by substituting the total inorganic carbon, $[CO_3^{2-}]_{outlet}$, $\Delta[Ca^{2+}]$ and $[Cl^{-1}] = 2\Delta[Ca^{2+}]$ back into Minteq and run at 60 ^oC and the calculated outlet pH was determined after running Minteq using the concentration determined at 25 ^oC

Table 7.3: Experimental results for solution saturation state, Ω_{inlet} = 0.12 of pH = 8.12 using 360 µm (un-etched) crystals at a flow rate of 6.8mL/hr.

Time hr	$[Ca^{2+}]_{inlet}$ Ppm	$[Ca^{2+}]_{outlet}$ ppm	$\Delta[Ca^{2+}]$ ppm	Expt. outlet pH at 25 ºC	Calc. outlet pH at 25 ºC	Ω_{outlet} at 60 ºC	$[CO_3^{2-}]_{outlet}$ Molar	Rate mol/cm^2/s	Rate uncertainty
3	0.41	1.21	0.80	8.13	8.29	0.91	1.20E-03	1.03E-11	7.14E-13
8	0.42	1.20	0.78	8.13	8.29	0.88	1.20E-03	1.00E-11	6.97E-13
13	0.40	1.11	0.71	8.13	8.29	0.77	1.20E-03	9.13E-12	6.36E-13
27	0.40	1.00	0.60	8.13	8.25	0.63	1.10E-03	7.72E-12	5.43E-13
32	0.42	0.99	0.57	8.12	8.25	0.59	1.10E-03	7.33E-12	5.17E-13
37	0.42	0.97	0.55	8.12	8.25	0.56	1.10E-03	7.07E-12	5.00E-13
48	0.40	0.82	0.42	8.12	8.25	0.49	1.10E-03	5.40E-12	3.92E-13
56	0.41	0.75	0.34	8.12	8.25	0.34	1.10E-03	4.37E-12	3.27E-13
61	0.43	0.75	0.32	8.12	8.25	0.26	1.10E-03	4.12E-12	3.10E-13
75	0.42	0.70	0.28	8.12	8.25	0.26	1.10E-03	3.60E-12	2.79E-13
80	0.42	0.68	0.26	8.12	8.25	0.29	1.10E-03	3.34E-12	2.75E-13
85	0.42	0.66	0.24	8.12	8.25	0.26	1.10E-03	3.09E-12	2.61E-13
99	0.43	0.68	0.25	8.12	8.25	0.26	1.10E-03	3.22E-12	2.68E-13
104	0.42	0.66	0.24	8.12	8.25	0.26	1.10E-03	3.09E-12	2.61E-13
109	0.42	0.66	0.24	8.12	8.25	0.26	1.10E-03	3.09E-12	2.61E-13
121	0.41	0.64	0.23	8.12	8.25	0.26	1.10E-03	2.96E-12	2.29E-13
126	0.43	0.66	0.23	8.12	8.25	0.26	1.10E-03	2.96E-12	2.29E-13
130	0.43	0.66	0.23	8.12	8.25	0.26	1.10E-03	2.96E-12	2.29E-13
141	0.43	0.66	0.23	8.12	8.25	0.25	1.10E-03	2.96E-12	2.29E-13
146	0.43	0.66	0.23	8.12	8.25	0.26	1.10E-03	2.96E-12	2.29E-13

Table 7.4: Experimental results for solution saturation state, Ω_{inlet} = 0.15 of pH = 8.14 using 160 µm (un-etched) crystals at a flow rate of 3.4mL/hr.

Time hr	$[Ca^{2+}]_{inlet}$ Ppm	$[Ca^{2+}]_{outlet}$ ppm	$\Delta[Ca^{2+}]$ ppm	Expt. outlet pH at 25 ºC	Calc. outlet pH at 25 ºC	Ω_{outlet} at 60 ºC	$[CO_3^{2-}]_{outlet}$ Molar	Rate mol/cm^2/s	Rate uncertainty
3	0.46	3.41	2.95	8.18	8.32	0.89	1.30E-03	8.81E-12	3.82E-13
8	0.44	2.32	1.88	8.16	8.32	0.58	1.30E-03	5.62E-12	2.44E-13
13	0.43	2.09	1.66	8.14	8.32	0.51	1.30E-03	4.96E-12	2.15E-13
27	0.44	1.88	1.44	8.14	8.32	0.44	1.30E-03	4.30E-12	1.87E-13
32	0.43	1.78	1.35	8.14	8.33	0.42	1.30E-03	4.03E-12	1.75E-13
37	0.43	1.70	1.27	8.12	8.33	0.39	1.30E-03	3.79E-12	1.65E-13
48	0.43	1.50	1.07	8.12	8.33	0.33	1.30E-03	3.20E-12	1.39E-13
56	0.43	1.26	0.83	8.12	8.33	0.26	1.30E-03	2.48E-12	1.08E-13
61	0.44	1.20	0.76	8.12	8.33	0.24	1.30E-03	2.27E-12	9.87E-14
75	0.44	1.00	0.56	8.12	8.33	0.17	1.30E-03	1.67E-12	7.29E-14
80	0.44	0.90	0.46	8.12	8.33	0.15	1.30E-03	1.37E-12	6.95E-14
85	0.43	0.84	0.41	8.12	8.33	0.13	1.30E-03	1.22E-12	6.42E-14
99	0.44	0.82	0.38	8.12	8.33	0.12	1.30E-03	1.14E-12	6.09E-14
104	0.43	0.80	0.37	8.12	8.33	0.12	1.30E-03	1.11E-12	5.99E-14
109	0.41	0.79	0.38	8.12	8.33	0.11	1.30E-03	1.14E-12	6.09E-14
121	0.44	0.78	0.34	8.12	8.33	0.11	1.30E-03	1.02E-12	5.68E-14
126	0.46	0.72	0.26	8.12	8.33	0.10	1.30E-03	7.77E-13	4.91E-14
130	0.42	0.79	0.37	8.12	8.33	0.12	1.30E-03	1.11E-12	5.99E-14
141	0.42	0.76	0.34	8.12	8.33	0.11	1.30E-03	1.02E-12	5.68E-14
146	0.42	0.75	0.33	8.12	8.33	0.11	1.30E-03	9.86E-13	5.59E-14
151	0.47	0.74	0.27	8.12	8.33	0.10	1.30E-03	8.07E-13	4.12E-14
162	0.49	0.73	0.24	8.12	8.33	0.10	1.30E-03	7.17E-13	3.79E-14
167	0.51	0.72	0.21	8.12	8.33	0.10	1.30E-03	6.27E-13	3.48E-14
179	0.51	0.71	0.20	8.12	8.33	0.10	1.30E-03	5.97E-13	3.38E-14
184	0.49	0.71	0.22	8.12	8.33	0.10	1.30E-03	6.57E-13	3.59E-14

Table 7.5: Experimental results for solution saturation state, Ω_{inlet} = 0.15 of pH = 8.14 using 360 µm (un-etched) crystals at a flow rate of 3.4mL/hr.

Time	$[Ca^{2+}]_{inlet}$	$[Ca^{2+}]_{outlet}$	$\Delta[Ca^{2+}]$	Expt. outlet	Calc. outlet	Ω_{outlet} at	$[CO_3^{2-}]_{outlet}$	Rate	Rate
hr	Ppm	ppm	ppm	pH at 25 ºC	pH at 25 ºC	60 ºC	Molar	mol/cm^2/s	uncertainty
3	0.79	2.11	1.32	8.16	8.29	0.57	1.20E-03	8.49E-12	5.87E-13
8	0.79	1.57	0.78	8.15	8.34	0.54	1.40E-03	5.02E-12	3.56E-13
1	0.77	1.63	0.86	8.14	8.34	0.56	1.40E-03	5.53E-12	3.89E-13
27	0.77	1.57	0.80	8.14	8.34	0.57	1.40E-03	5.14E-12	3.64E-13
32	0.78	1.82	1.04	8.13	8.34	0.63	1.40E-03	6.69E-12	4.67E-13
37	0.82	1.42	0.60	8.13	8.33	0.38	1.30E-03	3.86E-12	2.81E-13
48	0.74	1.22	0.48	8.13	8.34	0.49	1.40E-03	3.09E-12	2.27E-13
56	0.77	1.15	0.38	8.13	8.33	0.36	1.30E-03	2.44E-12	1.87E-13
61	0.78	1.15	0.37	8.13	8.33	0.36	1.30E-03	2.38E-12	1.83E-13
75	0.78	1.15	0.37	8.13	8.33	0.36	1.30E-03	2.38E-12	1.83E-13
80	0.82	1.11	0.29	8.14	8.33	0.34	1.30E-03	1.86E-12	1.53E-13
85	0.8	1.10	0.30	8.13	8.33	0.34	1.30E-03	1.93E-12	1.47E-13
99	0.75	1.04	0.29	8.15	8.33	0.32	1.30E-03	1.86E-12	1.43E-13
104	0.75	1.03	0.28	8.13	8.33	0.32	1.30E-03	1.80E-12	1.39E-13
109	0.78	1.02	0.24	8.13	8.33	0.32	1.30E-03	1.54E-12	1.24E-13
121	0.78	1.00	0.22	8.13	8.33	0.31	1.30E-03	1.41E-12	1.17E-13
126	0.65	0.99	0.34	8.13	8.33	0.31	1.30E-03	2.19E-12	1.62E-13
130	0.68	0.99	0.31	8.13	8.33	0.31	1.30E-03	1.99E-12	1.50E-13
141	0.68	0.96	0.28	8.13	8.33	0.30	1.30E-03	1.80E-12	1.38E-13
146	0.66	0.96	0.30	8.13	8.33	0.30	1.30E-03	1.93E-12	1.46E-13
151	0.66	0.97	0.31	8.13	8.33	0.30	1.30E-03	1.99E-12	1.50E-13
162	0.65	0.96	0.31	8.13	8.33	0.30	1.30E-03	1.99E-12	1.49E-13
167	0.63	0.96	0.33	8.13	8.33	0.30	1.30E-03	2.12E-12	1.57E-13
179	0.64	0.94	0.30	8.13	8.33	0.29	1.30E-03	1.93E-12	1.46E-13
184	0.69	0.95	0.26	8.13	8.33	0.29	1.30E-03	1.67E-12	1.30E-13
189	0.71	0.94	0.23	8.13	8.33	0.29	1.30E-03	1.48E-12	1.18E-13
200	0.71	0.92	0.21	8.13	8.33	0.29	1.30E-03	1.35E-12	1.11E-13
205	0.71	0.93	0.22	8.13	8.33	0.29	1.30E-03	1.41E-12	1.14E-13

Table 7.6: Experimental results for solution saturation state, Ω_{inlet} = 0.15 of pH = 8.14 using 360 µm (10 min etched) crystals at a flow rate of 3.4mL/hr.

Time hr	$[Ca^{2+}]_{inlet}$ Ppm	$[Ca^{2+}]_{outlet}$ ppm	$\Delta[Ca^{2+}]$ ppm	Expt. outlet pH at 25 °C	Calc. outlet pH at 25 °C	Ω_{outlet} at 60 °C	$[CO_3^{2-}]_{outlet}$ Molar	Rate mol/cm^2/s	Rate uncertainty
3	0.67	2.13	1.46	8.18	8.32	0.65	1.40E-03	9.39E-12	6.48E-13
8	0.67	1.80	1.13	8.19	8.35	0.62	1.40E-03	7.27E-12	5.05E-13
13	0.72	1.75	1.03	8.19	8.35	0.61	1.40E-03	6.62E-12	4.63E-13
27	0.73	1.75	1.02	8.18	8.35	0.61	1.40E-03	6.56E-12	4.58E-13
32	0.72	1.73	1.01	8.19	8.35	0.59	1.40E-03	6.49E-12	4.54E-13
37	0.72	1.55	0.83	8.17	8.35	0.54	1.40E-03	5.34E-12	3.77E-13
48	0.70	1.55	0.85	8.19	8.35	0.54	1.40E-03	5.47E-12	3.86E-13
56	0.70	1.39	0.69	8.19	8.33	0.43	1.30E-03	4.44E-12	3.19E-13
61	0.69	1.38	0.69	8.18	8.33	0.43	1.30E-03	4.44E-12	3.19E-13
75	0.75	1.39	0.64	8.18	8.33	0.43	1.30E-03	4.12E-12	2.98E-13
80	0.71	1.16	0.45	8.18	8.33	0.36	1.30E-03	2.89E-12	2.29E-13
85	0.69	1.14	0.45	8.18	8.33	0.36	1.30E-03	2.89E-12	2.29E-13
99	0.72	1.15	0.43	8.18	8.33	0.36	1.30E-03	2.77E-12	2.22E-13
104	0.71	1.08	0.37	8.18	8.33	0.33	1.30E-03	2.38E-12	1.99E-13
109	0.68	1.08	0.40	8.16	8.33	0.33	1.30E-03	2.57E-12	2.10E-13
121	0.70	1.06	0.36	8.17	8.33	0.33	1.30E-03	2.31E-12	1.96E-13
126	0.69	1.07	0.38	8.17	8.33	0.33	1.30E-03	2.44E-12	2.03E-13
130	0.74	1.07	0.33	8.17	8.33	0.33	1.30E-03	2.12E-12	1.86E-13
141	0.75	1.06	0.31	8.17	8.33	0.33	1.30E-03	1.99E-12	1.79E-13
146	0.74	0.96	0.22	8.17	8.33	0.30	1.30E-03	1.41E-12	1.51E-13
151	0.73	1.00	0.27	8.17	8.33	0.31	1.30E-03	1.74E-12	1.61E-13
162	0.70	1.00	0.30	8.17	8.33	0.31	1.30E-03	1.93E-12	1.71E-13
167	0.67	0.98	0.31	8.17	8.33	0.30	1.30E-03	1.99E-12	1.74E-13
179	0.68	0.95	0.27	8.17	8.33	0.30	1.30E-03	1.74E-12	1.61E-13
184	0.68	0.94	0.26	8.17	8.33	0.30	1.30E-03	1.67E-12	1.58E-13
189	0.68	0.93	0.25	8.17	8.33	0.29	1.30E-03	1.61E-12	1.55E-13
200	0.68	0.89	0.21	8.18	8.33	0.27	1.30E-03	1.35E-12	1.43E-13

Table 7.7: Experimental results for solution saturation state, Ω_{inlet} = 0.25 of pH = 8.18 using 360 µm (un-etched) crystals at a flow rate of 3.4mL/hr.

Time hr	$[Ca^{2+}]_{inlet}$ Ppm	$[Ca^{2+}]_{outlet}$ ppm	$\Delta[Ca^{2+}]$ ppm	Expt. outlet pH at 25 ºC	Calc. outlet pH at 25 ºC	Ω_{outlet} at 60 ºC	$[CO_3^{2-}]_{outlet}$ Molar	Rate mol/cm^2/s	Rate uncertainty
3	1.12	1.97	0.85	8.24	8.59	0.68	2.50E-03	5.47E-12	3.78E-13
8	1.28	1.94	0.66	8.24	8.59	0.69	2.50E-03	4.24E-12	2.96E- 3
13	1.18	1.80	0.62	8.24	8.59	0.51	2.50E-03	3.99E-12	2.79E-13
27	1.11	1.48	0.37	8.23	8.59	0.49	2.50E-03	2.38E-12	1.74E-13
32	1.18	1.39	0.21	8.23	8.59	0.46	2.40E-03	1.35E-12	1.11E-13
37	1.07	1.58	0.51	8.24	8.59	0.42	2.50E-03	3.28E-12	2.32E-13
48	1.11	1.35	0.24	8.23	8.58	0.38	2.40E-03	1.54E-12	1.22E-13
56	1.05	1.29	0.24	8.23	8.58	0.36	2.40E-03	1.54E-12	1.22E-13
61	1.07	1.33	0.26	8.23	8.58	0.34	2.40E-04	1.67E-12	1.30E-13
75	1.08	1.30	0.22	8.23	8.58	0.32	2.40E-04	1.41E-12	1.15E-13
80	1.03	1.23	0.20	8.23	8.58	0.31	2.40E-04	1.29E-12	1.08E-13
85	1.07	1.24	0.17	8.23	8.58	0.28	2.40E-04	1.09E-12	9.74E-14
99	1.03	1.22	0.19	8.23	8.58	0.27	2.40E-04	1.22E-12	1.04E-13
104	1.07	1.14	0.07	8.23	8.58	0.25	2.00E-04	4.50E-13	6.97E-14

Table 7.8: Experimental results for solution saturation state, Ω_{inlet} = 0.32 of pH = 8.20 using 360 µm (un-etched) crystals at a flow rate of 3.4mL/hr.

Time hr	$[Ca^{2+}]_{inlet}$ Ppm	$[Ca^{2+}]_{outlet}$ ppm	$\Delta[Ca^{2+}]$ ppm	Expt. outlet pH at 25 ºC	Calc. outlet pH at 25 ºC	Ω_{outlet} at 60 ºC	$[CO_3^{2-}]_{outlet}$ Molar	Rate mol/cm^2/s	Rate uncertainty
3	1.02	1.92	0.90	8.14	8.60	0.81	2.80E-03	5.79E-12	3.97E-13
8	1.01	1.70	0.69	8.14	8.60	0.67	2.60E-03	4.44E-12	3.05E-13
13	1.00	1.59	0.59	8.13	8.59	0.57	2.50E-03	3.79E-12	2.61E-13
27	1.00	1.41	0.41	8.13	8.59	0.53	2.50E-03	2.64E-12	1.82E-13
32	1.01	1.25	0.24	8.13	8.59	0.52	2.50E-03	1.54E-12	1.07E-13
37	0.99	1.20	0.21	8.13	8.59	0.49	2.50E-03	1.35E-12	9.37E-14
48	0.97	1.16	0.19	8.12	8.59	0.47	2.50E-03	1.22E-12	8.49E-14
56	1.01	1.13	0.12	8.12	8.59	0.46	2.50E-03	7.72E-13	5.36E-14
61	1.01	1.13	0.12	8.12	8.59	0.44	2.50E-03	7.72E13	5.36E-14
75	0.98	1.16	0.18	8.12	8.59	0.44	2.50E-03	1.16E-12	8.04E-14
80	1.03	1.12	0.09	8.12	8.59	0.41	2.50E-03	5.79E-13	4.02E-14
85	1.04	1.10	0.06	8.12	8.59	0.39	2.50E-03	3.86E-13	2.68E-14
99	1.06	1.09	0.03	8.12	8.59	0.38	2.40E-03	1.93E-13	1.34E-14
104	1.05	1.09	0.04	8.12	8.59	0.36	2.40E-03	2.57E-13	1.79E-14
109	1.04	1.09	0.05	8.12	8.59	0.35	2.40E-03	3.22E-13	2.248E-14

Table 7.9: Experimental results for solution saturation state, Ω_{inlet} = 0.32 of pH = 8.19 using 360 µm (1 min etched) crystals at a flow rate of 3.4mL/hr.

Time hr	$[Ca^{2+}]_{inlet}$ Ppm	$[Ca^{2+}]_{outlet}$ ppm	$\Delta[Ca^{2+}]$ ppm	Expt. outlet pH at 25 ºC	Calc. outlet pH at 25 ºC	Ω_{outlet} at 60 ºC	$[CO_3^{2-}]_{outlet}$ Molar	Rate mol/cm^2/s	Rate uncertainty
3	1.05	2.07	1.02	8.15	8.41	0.87	1.60E-03	6.56E-12	4.55E-13
8	1.00	1.65	0.65	8.13	8.38	0.65	1.50E-03	4.18E-12	2.97E-13
13	0.99	1.58	0.59	8.13	8.38	0.60	1.50E-03	3.79E-12	2.72E-13
27	1.00	1.35	0.35	8.12	8.38	0.52	1.50E-03	2.25E-12	1.74E-13
32	1.03	1.36	0.33	8.12	8.38	0.52	1.50E-03	2.12E-12	1.66E-13
37	1.03	1.23	0.20	8.12	8.38	0.48	1.50E-03	1.29E-12	1.20E-13
48	1.03	1.22	0.19	8.12	8.38	0.48	1.50E-03	1.22E-12	1.17E-13
56	1.01	1.19	0.18	8.12	8.38	0.46	1.50E-03	1.16E-12	1.14E-13
61	1.03	1.14	0.11	8.11	8.38	0.44	1.50E-03	7.07E-13	9.55E-14
75	1.05	1.17	0.12	8.11	8.38	0.46	1.50E-03	7.72E-13	9.78E-14
80	1.03	1.11	0.08	8.11	8.38	0.39	1.40E-03	5.14E-13	8.96E-14
85	1.04	1.12	0.08	8.11	8.38	0.39	1.40E-03	5.14E-13	8.96E-14
99	1.01	1.11	0.10	8.11	8.38	0.39	1.40E-03	6.43E-13	9.34E-14
104	1.04	1.11	0.07	8.11	8.38	0.39	1.40E-03	4.50E-13	8.79E-14
109	1.02	1.11	0.09	8.11	8.38	0.39	1.40E-03	5.79E-13	9.14E-14
121	1.01	1.09	0.08	8.11	8.38	0.38	1.40E-03	5.14E-13	8.97E-14
126	1.03	1.08	0.05	8.11	8.38	0.38	1.40E-03	3.22E-13	8.54E-14
130	1.02	1.08	0.06	8.11	8.38	0.38	1.40E-03	3.86E-13	8.66E-14

Table 7.10: Experimental results for solution saturation state, Ω_{inlet} = 0.32 of pH = 8.18 using 360 µm (100 min etched) crystals at a flow rate of 3.4mL/hr.

Time hr	$[Ca^{2+}]_{inlet}$ Ppm	$[Ca^{2+}]_{outlet}$ ppm	$\Delta[Ca^{2+}]$ ppm	Expt. outlet pH at 25 ºC	Calc. outlet pH at 25 ºC	Ω_{outlet} at 60 ºC	$[CO_3^{2-}]_{outlet}$ Molar	Rate mol/cm^2/s	Rate Uncertainty
3	1.01	2.47	1.46	8.14	8.36	0.85	1.40E-03	9.39E-12	6.55E-13
8	1 01	2.45	1.44	8.14	8.36	0.83	1.40E-03	9.26E-12	6.47E-13
13	1.02	2.31	1.29	8.13	8.36	0.81	1.40E-03	8.30E-12	5.83E-13
27	0.98	2.02	1.04	8.13	8.33	0.69	1.30E-03	6.69E-12	4.77E-13
32	0.99	1.70	0.71	8.13	8.32	0.52	1.30E-03	4.57E-12	3.42E-13
37	1.04	1.71	0.67	8.13	8.32	0.52	1.30E-03	4.31E-12	3.26E-13
48	1.03	1.66	0.63	8.12	8.32	0.51	1.30E-03	4.05E-12	3.10E-13
56	1.01	1.59	0.58	8.12	8.32	0.49	1.30E-03	3.73E-12	2.91E-13
61	1.04	1.55	0.51	8.12	8.32	0.48	1.30E-03	3.28E-12	2.64E-13
75	0.99	1.54	0.55	8.12	8.32	0.48	1.30E-03	3.54E-12	2.79E-13
80	1.03	1.47	0.44	8.12	8.32	0.46	1.30E-03	2.83E-12	2.39E-13
85	1.03	1.45	0.42	8.12	8.32	0.43	1.30E-03	2.70E-12	2.32E-13
99	1.03	1.37	0.34	8.12	8.32	0.43	1.30E-03	2.19E-12	2.05E-13
104	1.02	1.28	0.26	8.12	8.32	0.40	1.30E-03	1.67E-12	1.82E-13
109	1.04	1.23	0.19	8.12	8.32	0.38	1.30E-03	1.22E-12	1.64E-13
121	1.04	1.12	0.08	8.12	8.32	0.35	1.30E-03	5.14E-13	1.46E-13
126	1.03	1.12	0.09	8.12	8.32	0.35	1.30E-03	5.79E-13	1.47E-13
130	1.01	1.14	0.13	8.12	8.32	0.35	1.30E-03	8.36E-13	1.53E-13

Table 7.11: Experimental results for solution saturation state, Ω_{inlet} = 0.56 of pH = 8.24 using 360 µm (un-etched) crystals at a flow rate of 3.4mL/hr.

Time hr	$[Ca^{2+}]_{inlet}$ Ppm	$[Ca^{2+}]_{outlet}$ ppm	$\Delta[Ca^{2+}]$ ppm	Exp. outlet pH at 25 ºC	Calc. outlet pH at 25 ºC	Ω_{outlet} at 60 ºC	$[CO_3^{2-}]_{outlet}$ Molar	Rate mol/cm^2/s	Rate uncertainty
3	1.83	1.94	0.11	8.43	8.52	0.77	2.10E-03	7.07E-13	1.03E-13
8	1.85	1.93	0.08	8.43	8.52	0.76	2.10E-03	5.14E-13	9.71E-14
1	1.82	1.94	0.12	8.43	8.52	0.76	2.10E-03	7.72E-13	1.05E-13
27	1.80	1.93	0.13	8.43	8.52	0.77	2.10E-03	8.36E-13	1.07E-13
32	1.81	1.93	0.12	8.43	8.52	0.77	2.10E-03	7.72E-13	1.05E-13
37	1.82	1.94	0.12	8.41	8.52	0.77	2.10E-03	7.72E-13	1.05E-13
48	1.83	1.95	0.12	8.41	8.52	0.77	2.10E-03	7.72E-13	1.05E-13
56	1.81	1.93	0.12	8.41	8.52	0.77	2.10E-03	7.72E-13	1.05E-13
61	1.82	1.94	0.12	8.41	8.52	0.77	2.10E-03	7.72E-13	1.05E-13
75	1.81	1.90	0.09	8.41	8.52	0.76	2.10E-03	5.79E-13	9.88E-14
80	1.83	1.90	0.07	8.41	8.52	0.74	2.07E-03	4.50E-13	9.51E-14
85	1.83	1.93	0.10	8.41	8.50	0.76	2.07E-07	6.43E-13	1.01E-13
99	1.82	1.87	0.05	8.41	8.50	0.71	2.00E-03	3.22E-13	9.32E-14
104	1.84	1.88	0.04	8.41	8.50	0.69	2.00E-03	2.57E-13	9.22E-14
109	1.84	1.87	0.03	8.41	8.50	0.68	2.00E-03	1.93E-13	9.15E-14
121	1.84	1.87	0.03	8.41	8.50	0.68	2.00E-03	1.93E-13	9.15E-14
126	1.82	1.84	0.02	8.41	8.50	0.66	2.00E-03	1.29E-13	9.10E-14
130	1.80	1.85	0.05	8.39	8.50	0.71	2.00E-03	3.22E-13	9.32E-14
141	1.82	1.84	0.02	8.39	8.50	0.66	2.00E-03	1.29E-13	9.10E-14
146	1.81	1.84	0.03	8.39	8.50	0.68	2.00E-03	1.93E-13	9.63E-14
151	1.85	1.87	0.02	8.39	8.50	0.66	2.00E-03	1.29E-13	5.94E-14

Table 7.12: Experimental results for solution saturation state, Ω_{inlet} = 0.56 of pH = 8.24 using 360 μm (0 min etched) crystals at a flow rate of 3.4mL/hr.

Time hr	$[Ca^{2+}]_{inlet}$ Ppm	$[Ca^{2+}]_{outlet}$ ppm	$\Delta[Ca^{2+}]$ ppm	Expt. outlet pH at 25 ºC	Calc. outlet pH at 25 ºC	Ω_{outlet} at 60 ºC	$[CO_3^{2-}]_{outlet}$ Molar	Rate mol/cm^2/s	Rate uncertainty
3	1.81	1.86	0.05	8.40	8.50	0.70	2.00E-03	3.22E-13	5.81E-14
8	1.83	1.87	0.04	8.40	8.50	0.69	2.00E-03	2.57E-13	5.66E-14
13	1.80	1.85	0.05	8.40	8.50	0.71	2.00E-03	3.22E-13	5.81E-14
27	1.81	1.83	0.02	8.40	8.50	0.66	2.00E-03	1.29E-13	5.45E-14
32	1.81	1.86	0.05	8.39	8.50	0.71	2.00E-03	3.22E-13	5.81E-14
37	1.78	1.83	0.05	8.39	8.50	0.71	2.00E-03	3.22E-13	5.81E-14
48	1.81	1.83	0.02	8.39	8.50	0.66	2.00E-03	1.29E-13	5.45E-14
56	1.78	1.83	0.05	8.39	8.50	0.71	2.00E-03	3.22E-13	5.81E-14
61	1.80	1.82	0.02	8.39	8.50	0.66	2.00E-03	1.29E-13	5.45E-14
75	1.79	1.82	0.03	8.39	8.50	0.68	2.00E-03	1.93E-13	5.54E-14
80	1.78	1.83	0.05	8.39	8.50	0.71	2.00E-03	3.22E-13	5.81E-14
85	1.81	1.84	0.03	8.39	8.50	0.68	2.00E-03	1.93E-13	5.54E-14
99	1.80	1.85	0.05	8.39	8.50	0.71	2.00E-03	3.22E-13	5.81E-14
104	1.80	1.82	0.02	8.39	8.50	0.66	2.00E-03	1.29E-13	5.45E-14
109	1.82	1.84	0.02	8.39	8.50	0.66	2.00E-03	1.29E-13	5.45E-14
121	1.81	1.83	0.02	8.39	8.50	0.66	2.00E-03	1.29E-13	5.45E-14
126	1.83	1.85	0.02	8.39	8.50	0.66	2.00E-03	1.29E-13	5.45E-14
130	1.83	1.85	0.02	8.39	8.50	0.66	2.00E-03	1.29E-13	5.45E-14
141	1.80	1.84	0.04	8.39	8.50	0.69	2.00E-03	2.57E-13	3.92E-14
146	1.80	1.83	0.03	8.39	8.50	0.68	2.00E-03	1.93E-13	3.75E-14

Table 7.13: Experimental results for solution saturation state, Ω_{inlet} = 0.56 of pH = 8.22 using 360 µm (10 min etched) crystals at a flow rate of 3.4mL/hr.

Time hr	$[Ca^{2+}]_{inlet}$ Ppm	$[Ca^{2+}]_{outlet}$ ppm	$\Delta[Ca^{2+}]$ ppm	Expt. outlet pH at 25 ºC	Calc. outlet pH at 25 ºC	Ω_{outlet} at 60 ºC	$[CO_3^{2-}]_{outlet}$ Molar	Rate mol/cm^2/s	Rate uncertainty
3	1.83	2.19	0.36	8.39	8.52	0.69	2.20E-03	2.31E-12	1.65E-13
8	1.85	2.17	0.32	8.39	8.52	0.68	2.13E-03	2.06E-12	1.48E-13
13	1.85	2.16	0.31	8.39	8.52	0.68	2.10E-03	1.99E-12	1.44E-13
27	1.84	2.10	0.26	8.39	8.52	0.66	2.10E-03	1.67E-12	1.23E-13
32	1.82	2.04	0.22	8.39	8.52	0.65	2.10E-03	1.41E-12	1.07E-13
37	1.80	1.98	0.18	8.39	8.52	0.65	2.10E-03	1.16E-12	9.16E-14
48	1.83	2.00	0.17	8.39	8.52	0.64	2.10E-03	1.09E-12	8.79E-14
56	1.80	1.98	0.18	8.39	8.52	0.65	2.10E-03	1.16E-12	9.16E-14
61	1.81	1.95	0.14	8.39	8.52	0.63	2.10E-03	9.00E-13	7.71E-14
75	1.80	1.91	0.11	8.39	8.52	0.62	2.10E-03	7.07E-13	6.70E-14
80	1.79	1.91	0.12	8.39	8.52	0.62	2.10E-03	7.72E-13	6.82E-14
85	1.82	1.90	0.08	8.39	8.52	0.60	2.10E-03	5.14E-13	5.58E-14
99	1.81	1.85	0.06	8.39	8.52	0.59	2.10E-03	2.57E13	4.67E-14
104	1.83	1.88	0.05	8.39	8.52	0.58	2.10E-03	3.22E-13	4.86E-14
109	1.82	1.86	0.04	8.39	8.52	0.57	2.10E-03	2.57E-13	4.68E-14
121	1.84	1.87	0.03	8.39	8.52	0.56	2.10E-03	1.93E-13	4.16E-14
126	1.83	1.87	0.04	8.39	8.52	0.57	2.10E-03	2.57E-13	4.32E-14
130	1.83	1.86	0.03	8.39	8.52	0.56	2.10E-03	1.93E-13	4.16E-14
141	1.84	1.86	0.03	8.39	8.52	0.56	2.10E-03	1.29E-13	4.05E-14
146	1.83	1.87	0.04	8.39	8.52	0.57	2.10E-03	2.57E-13	4.32E-14

Table 7.14: Experimental results for solution saturation state, Ω_{inlet} = 0.56 of pH = 8.23 using 360 µm (100 min etched) crystals at a flow rate of 3.4mL/hr.

Time hr	$[Ca^{2+}]_{inlet}$ Ppm	$[Ca^{2+}]_{outlet}$ ppm	$\Delta[Ca^{2+}]$ Ppm	Expt. outlet pH at 25 ºC	Calc. outlet pH at 25 ºC	Ω_{outlet} at 60 ºC	$[CO_3^{2-}]_{outlet}$ Molar	Rate mol/cm^2/s	Rate uncertainty
3	1.80	2.44	0.64	0.39	8.58	0.74	2.40E-03	4.12E-12	2.92E-13
8	1.83	2.31	0.48	8.39	8.58	0.72	2.40E-03	3.09E-12	2.26E-13
13	1.83	2.34	0.51	8.39	8.58	0.72	2.40E-03	3.28E-12	2.38E-13
27	1.79	2.16	0.37	8.39	8.54	0.69	2.20E-03	2.38E-12	1.82E-13
32	1.82	2.09	0.27	8.39	8.54	0.68	2.20E-03	1.74E-12	1.44E-13
37	1.79	2.00	0.21	8.39	8.54	0.66	2.20E-03	1.35E-12	1.23E-13
48	1.82	1.92	0.10	8.39	8.52	0.62	2.20E-03	6.43E-13	9.28E-14
56	1.80	1.91	0.11	8.39	8.52	0.62	2.17E-03	7.07E-13	9.49E-14
61	1.82	1.93	0.11	8.39	8.52	0.62	2.17E-03	7.07E-13	9.49E-14
75	1.85	1.90	0.05	8.39	8.52	0.58	2.17E-03	3.22E-13	8.52E-14
80	1.78	1.91	0.13	8.39	8.52	0.62	2.17E-03	8.36E-13	1.00E-13
85	1.80	1.95	0.15	8.39	8.52	0.63	2.17E-03	9.65E-13	1.05E-13
99	1.81	1.92	0.11	8.39	8.52	0.62	2.17E-03	7.07E-13	9.55E-14
104	1.80	1.86	0.06	8.39	8.52	0.59	2.17E-03	3.86E-13	8.65E-14
109	1.79	1.88	0.09	8.39	8.52	0.60	2.17E-03	5.79E-13	9.13E-14
121	1.84	1.86	0.03	8.39	8.52	0.56	2.17E-03	1.29E-13	6.11E-14
126	1.85	1.87	0.03	8.39	8.52	0.56	2.17E-03	1.29E-13	6.12E-14
130	1.79	1.86	0.07	8.39	8.52	0.58	2.17E-03	4.50E-13	6.79E-14
141	1.83	1.85	0.03	8.39	8.52	0.56	2.17E-03	1.29E-13	6.12E-14
146	1.84	1.86	0.03	8.39	8.52	0.56	2.17E-03	1.29E-13	6.12E-14
151	1.80	1.85	0.05	8.39	8.52	0.58	2.17E-03	3.22E-13	6.44E-14

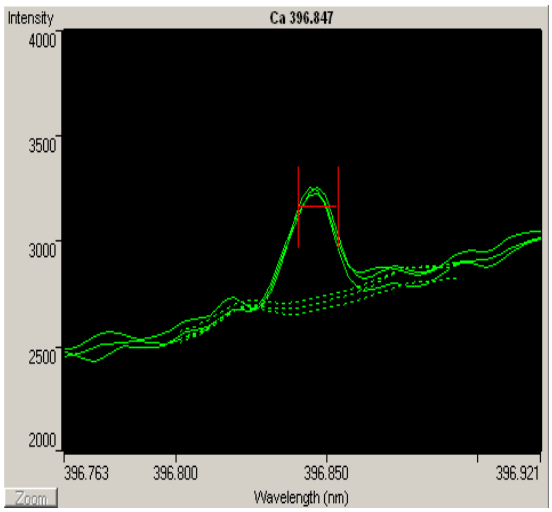

Blank

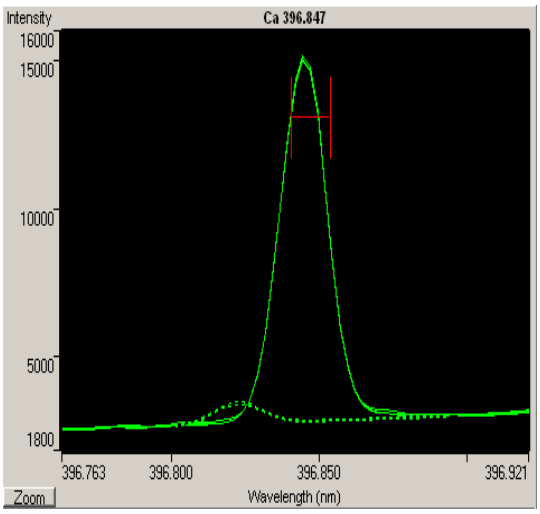

$[Ca^{2+}]$ = 5 ppb

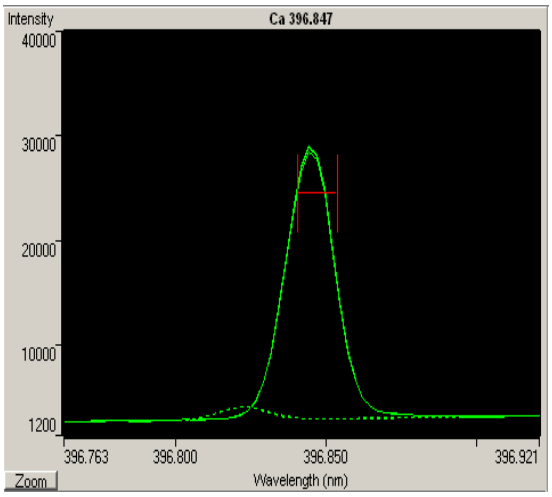

$[Ca^{2+}]$ = 10 ppb

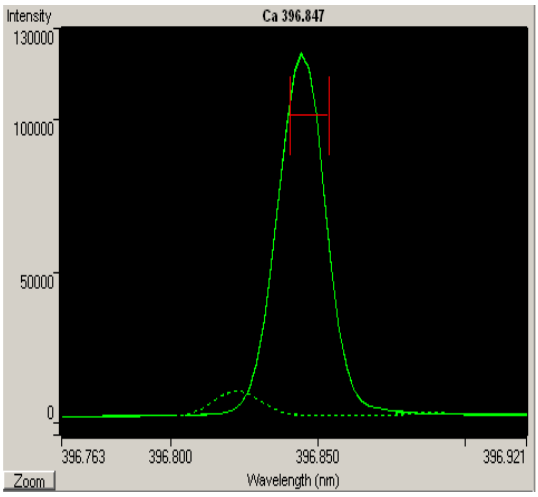

$[Ca^{2+}]$ = 50 ppb

Fig. 7.15: Calcium emission peaks of standards obtained from the ICP analysis. Triplicate analysis was performed on each standard and sample with a replicate read time of 3 min and sample delay uptake of 30 s. A rinsing time of 10 s was set between samples.

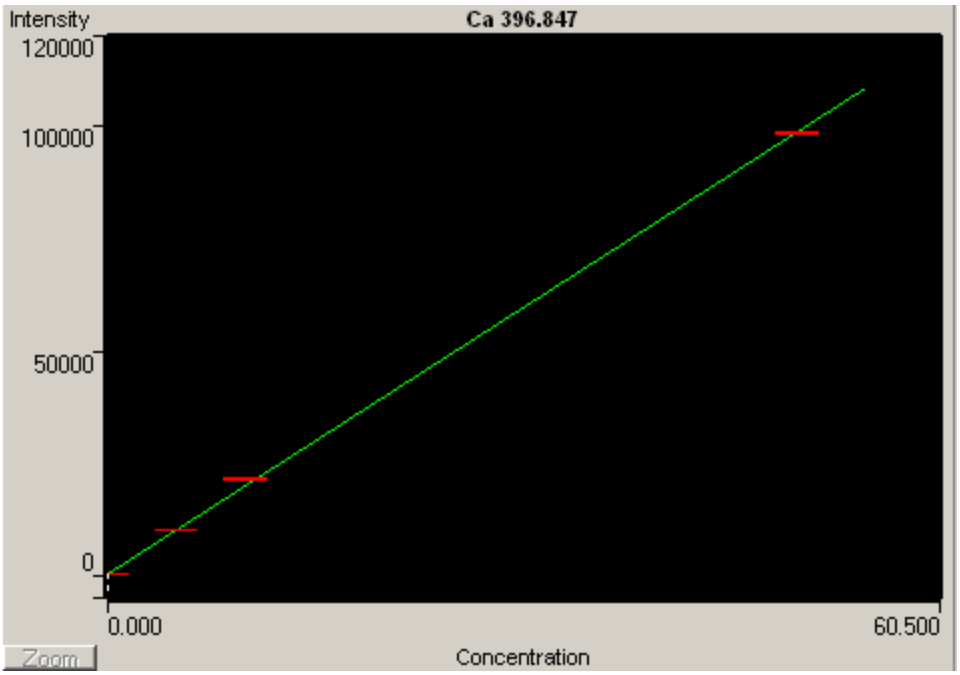

Fig. 7.16: Linear calibration curve of the standards for the ICP analysis of Ca^{2+} with a correlation coefficient of 0.997.

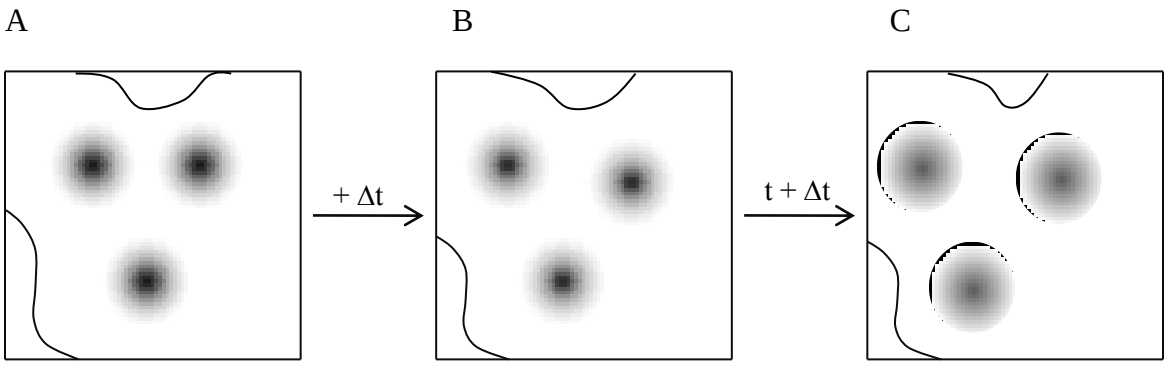

Fig. 7.17: A proposed model of topographic relaxation indicating the evolution of lateral dissolution in the etch pits from (A) to (C) with time where dissolution occurs via layer-by-layer removal of material on the terrace such that the pits become shallower.

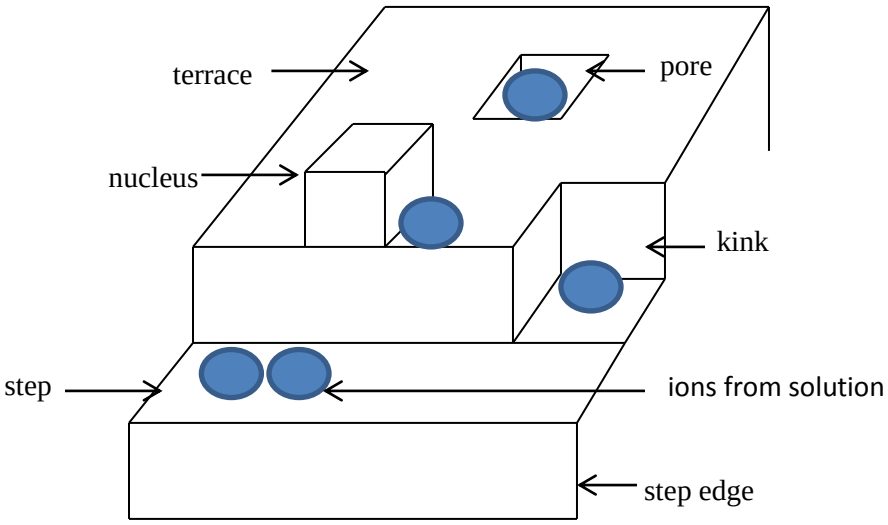

Fig. 7.18: A diagram representing the BCF model of calcite crystal surface showing the various surface sites that could undergo dissolution in the presence of aqueous solution.